Renormalization group analysis of Dirac fermions with a random mass

Zhiming Pan,[1] Tong Wang,[1] Tomi Ohtsuki,[2] and Ryuichi Shindou[1,*]
[1]*International Center for Quantum Materials, School of Physics, Peking University, Beijing 100871, China*
[2]*Physics Division, Sophia University, Chiyoda-ku, Tokyo 102-8554, Japan*

(Received 19 August 2021; revised 13 October 2021; accepted 8 November 2021; published 18 November 2021)

Two-dimensional (2D) disordered superconductor (SC) in class D exhibits a disorder-induced quantum multicritical phenomenon among diffusive thermal metal (DTM), topological superconductor (TS), and conventional localized (AI) phases. To characterize the quantum tricritical point where these three phases meet, we carry out a two-loop renormalization group (RG) analysis for 2D Dirac fermion with random mass in terms of the ϵ-expansion in the spatial dimension $d = 2 - \epsilon$. In two dimensions ($\epsilon = 0$), the random mass is marginally irrelevant around a clean-limit fixed point of the gapless Dirac fermion, while there exists an IR unstable fixed point at finite disorder strength that corresponds to the tricritical point. The critical exponent, dynamical exponent, and scaling dimension of the (uniform) mass term are evaluated around the tricritical point by the two-loop RG analysis. Using a mapping between an effective theory for the 2D random-mass Dirac fermion and the (1+1)-dimensional Gross-Neveu model, we further deduce the four-loop evaluation of the critical exponent, and the scaling dimension of the uniform mass around the tricritical point. Both the two-loop and four-loop results suggest that criticalities of a AI-DTM transition line as well as TS-DTM transition line are controlled by other saddle-point fixed point(s) at finite uniform mass.

DOI: 10.1103/PhysRevB.104.174205

I. INTRODUCTION

Low-energy fermionic excitation in p-wave superconductors with broken time-reversal and spin-rotational symmetries [1] has a "real-valued" character of its creation being identical to its annihilation (Majorana fermion). Such exotic excitations appear also as low-energy fractionalized magnetic excitations in certain quantum spin models [2], which could be realized in Mott insulators with heavy magnetic ions [3]. Experimental realizations of the Majorana particles acquire a lot of recent interests in condensed matter experiments, while it was suggested that quenched disorders may play crucial role in these experiments [4–9]. Two-dimensional (2D) class-D disordered superconductor (SC) models [10] are canonical models of Majorana quasiparticles in the presence of the disorder potentials. The class-D disordered SC models have three fundamental phases: topological superconductor (TS) phases with quantized thermal Hall conductance κ_{xy} in the unit of $\pi^2 k_B^2 T/6h$ (T is the temperature, k_B is the Boltzmann constant and h is the Plank constant) [11–13], a conventional superconductor or Anderson localized (AI) phase with $\kappa_{xy} = 0$, and a diffusive thermal metal (DTM) phase. Natures of quantum phase transitions among these three fundamental phases have been under active debate for decades, while a number of the numerical studies have been carried out on network models and lattice models [1,8,11,14–24].

A phase diagram of the class-D disordered SC models has a close connection with a phase diagram of a 2D $\pm J$ random bond Ising model (RBIM) [25–28]. In an exact mapping between the RBIM and disordered fermion models, the diffusive thermal metal phase is absent [1,14,16,29]. Cho and Fisher (CF) [11] found a mapping from the RBIM into a Chalker-Coddington network model (disordered fermion models) [30]. In the phase diagram of the CF network model, all the three fundamental phases appear and a TS-DTM transition line, AI-DTM transition line, and AI-TS transition line meet at a quantum tricritical point [16,18,19,21,24,31,32]. Critical exponents around the tricritical point have been evaluated numerically [21,24,31,32]. Previous numerical studies of the CF model also suggest a possibility of an additional fixed-point structure along the AI-TS transition line, which is seemingly related to a Nishimori point in the RBIM [16,18,19].

Theoretically, a low-energy effective theory of the class-D disordered SC models is described by a 2D Dirac fermion with random mass. Previous one-loop renormalization group (RG) analyses of the Dirac fermion with the random mass showed that the random mass is marginally irrelevant around a clean-limit fixed point (2D gapless Dirac fermion) [33,34]. Since the tricritical point is an infrared (IR) unstable fixed point at a finite disorder strength, a field-theoretical characterization of the tricritical point in the 2D class-D models needs a RG analysis of higher than one-loop level.

In this paper, we give a field-theoretical estimate of scaling properties of the tricritical point (TCP) and the three phase transition lines on the basis of the higher-loop RG analysis of the 2D Dirac fermion with the random Dirac mass. The 2D Dirac fermion is an effective theory for a topological phase transition between two topologically distinct gapped phases in a clean limit, where a change of a uniform Dirac mass term m induces the topological transition. The low-energy

*rshindou@pku.edu.cn

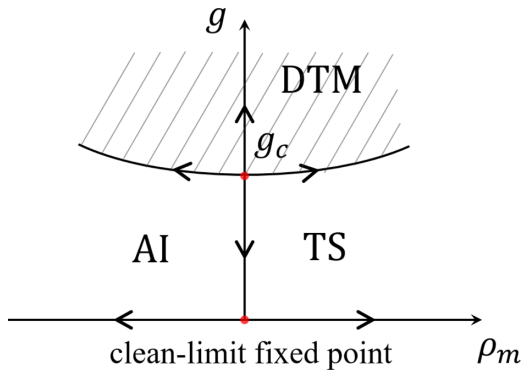

FIG. 1. Schematic phase diagram for one-component Dirac fermion with random Dirac mass. DTM is a diffusive thermal metal phase, TS and AI stand for a gapped phase with the nonzero topological integer ($C = -1$) and a gapped phase with zero topological integer ($C = 0$), respectively. The topological integers in the gapped phases characterize the thermal Hall conductivity as $\kappa_{xy} = C\pi^2 k_B^2 T/6h$. The vertical axis g represents the disorder strength of the Dirac-mass type and the horizontal axis represents the uniform Dirac mass m; ρ_m is a dimensionless renormalized mass. A critical point ($g = g_c$) at $\rho_m = 0$ is a tricritical point. The arrow stands for the renormalization group (RG) flow determined by the two-loop and four-loop RG analyses.

theory of the transition point in the clean limit is given by the 2D gapless Dirac fermion. Any onsite disorder potentials in the 2D gapless Dirac fermion are marginal around the clean-limit fixed point. Particle-hole symmetry in the class-D symmetry restricts a form of the disorders to be of the Dirac-mass type (random Dirac mass). The Dirac-mass type disorder is marginally irrelevant around the clean-limit fixed point [33,34]. In this paper, we demonstrate that an infrared (IR) unstable fixed point appears at a finite critical disorder strength, $g = g_c$ (Fig. 1), using the two-loop RG analyses and its extension up to the four-loop level. The IR unstable fixed point corresponds to the TCP, where the three phases in the class-D systems meet in their phase diagrams. From the clean-limit fixed point to the fixed point at $g = g_c$ runs a topological phase transition line, that intervenes between the two gapped phases; AI with $\kappa_{xy} = 0$ and TS with $\kappa_{xy} \neq 0$ (Fig. 1). We evaluate a scaling dimension of the uniform Dirac mass and dynamical exponent around the fixed point at $g = g_c$ at the two-loop level, and find that the uniform Dirac mass m as well as a deviation of the disorder strength from the critical disorder strength, $\delta g \equiv g - g_c$, are relevant scaling variables; Fig. 1. This determines the renormalization group (RG) flow around the TCP as well as the scaling properties of the three transition lines. Namely, the criticality of the TS-AI transition line is controlled by the clean-limit fixed point, while the criticalities of the DTM-TS phase transition and the DTM-AI phase transition are controlled by other theories with finite uniform mass m. Using a mapping between an effective model for the random-mass Dirac fermions and Gross-Neveu (GN) model together with preceding four-loop RG calculation of the GN model, we further discuss the scaling dimensions of the uniform mass m and the disorder strength δg around the TCP [35–37]. Both two-loop and four-loop results suggest that the tricritical point (TCP) is unstable in the IR limit (Fig. 1).

Disorder-driven quantum tricritical points appear also in phase diagrams of other 'Dirac' matters [38–40], such as three-dimensional (3D) Weyl/Dirac systems [38,39,41–50]. In the 3D disordered Weyl/Dirac systems, short-ranged disorders are irrelevant around a clean-limit fixed point (3D gapless Weyl/Dirac point) at the tree level, and the tricritical point at a finite disorder strength arises from a competition between the tree level term ("attractive" to the clean-limit fixed point) and one-loop level term ("repulsive") in a β function of the disorder strength. The key difference between the tricritical point in the 2D class-D Dirac matters and those in the 3D Weyl/Dirac matters stems from the particle-hole symmetry in the class-D symmetry that constrains the type of short-ranged disorders to be the Dirac mass type (random mass). Thereby, the random mass is marginally irrelevant at the one-loop level and a repulsive nature of RG flow appears only from the two-loop (and higher than the two-loop) level. A competition between the one-loop terms (attractive) and higher than one-loop terms (repulsive) in the β function of the random mass leads to the tricritical point in the 2D class-D Dirac systems.

The organization of this paper is as follows. In Sec. II, we introduce two-dimensional random-mass Dirac fermions as a low-energy theory for Bogoliubov excitations in a disordered $p_x + ip_y$ superconductor on a lattice. The theory has two controlled parameters; a disorder strength of the random-mass type, and the uniform mass that induces the topological phase transition between two gapped phases with distinct topological numbers. In Sec. III, we introduce an effective low-energy theory for the 2D random-mass Dirac fermions, generalize it in general spatial dimension d, and discuss the renormalizability of the effective theory in $d \leqslant 2$. In Sec. IV, we use minimal subtraction method in $d = 2 - \epsilon$ and derive two-loop renormalization group (RG) equations for the disorder strength. We obtain an anomalous dimension of the uniform mass as well as the dynamical exponent up to the two-loop level in Sec. IV. In Sec. V, we analyze the RG equation and obtain the critical disorder strength for the TCP, the scaling dimensions of the random mass and dynamical exponent around the TCP. In Sec. VI, we discuss a relation between the effective theory for the 2D random-mass Dirac fermions and (1+1)D SU(N) Gross-Neveu model. The relation gives the four-loop evaluations of the critical disorder strength g_c as well as scaling dimensions of the uniform mass m and disorder strength δg around the TCP. Section VII is devoted to summary and discussion.

II. TIGHT-BINDING MODEL OF SPINLESS $p_x + ip_y$ SUPERCONDUCTOR

A square-lattice model of spinless fermions with $p_x + ip_y$ Cooper pairing and the random chemical-potential type disorder is considered [51,52],

$$\mathcal{H}/2 = \sum_j (\varepsilon_j + \mu)\hat{c}_j^\dagger \hat{c}_j + t \sum_{j,\mu=x,y} [\hat{c}_{j+\boldsymbol{e}_\mu}^\dagger \hat{c}_j + \text{H.c.}] + \Delta \sum_j [i\hat{c}_{j+\boldsymbol{e}_x}^\dagger \hat{c}_j^\dagger + \hat{c}_{j+\boldsymbol{e}_y}^\dagger \hat{c}_j^\dagger + \text{H.c.}], \quad (1)$$

with uniform chemical potential μ, nearest-neighbor hopping amplitude t and superconducting pairing amplitude $\Delta \in \mathbb{R}$. Here $\boldsymbol{j} \equiv (j_x, j_y)$ denotes the lattice vectors, and $\boldsymbol{e}_x$ and $\boldsymbol{e}_y$ are primitive unit vectors in x and y direction, respectively. $\varepsilon_j \in [-W/2, W/2]$ is a short-ranged onsite chemical-potential-type random potential,

$$\langle \varepsilon_i \rangle_{\rm dis} = 0, \quad \langle \varepsilon_i \varepsilon_j \rangle_{\rm dis} = \delta_{i,j} W^2/12, \tag{2}$$

where $\langle \cdots \rangle_{\rm dis}$ stands for Gaussian disorder average. W represents the disorder strength of the random potential. With a two-components Nambu vector,

$$\Psi_j = \begin{pmatrix} \hat{c}_j \\ \hat{c}_j^\dagger \end{pmatrix}, \quad \Psi_j^\dagger = (\hat{c}_j^\dagger \quad \hat{c}_j), \tag{3}$$

the Hamiltonian in Eq. (1) is written as a Bogoliubov-de Gennes (BdG) form,

$$\begin{aligned} \mathcal{H} = & \sum_j \Psi_j^\dagger [\mathbb{H}]_{j,m} \Psi_m = \sum_j \Psi_j^\dagger [(\varepsilon_j + \mu)\sigma_3] \Psi_j \\ & + t \sum_j \sum_{\mu=x,y} [\Psi_{j+e_\mu}^\dagger (\sigma_3) \Psi_j + \text{H.c.}] \\ & + i\Delta \sum_j [\Psi_{j+e_x}^\dagger (\sigma_1) \Psi_j + \Psi_{j+e_y}^\dagger (\sigma_2) \Psi_j + \text{H.c.}] \end{aligned} \tag{4}$$

with the three Pauli matrices σ_i ($i = 1, 2, 3$). The BdG Hamiltonian in Eq. (4) satisfies a particle-hole symmetry,

$$\mathbb{C}\mathbb{H}^{\rm T}\mathbb{C}^{-1} = -\mathbb{H}, \tag{5}$$

with $[\mathbb{C}]_{j,m} = \delta_{j,m}\sigma_1$. The Hamiltonian also breaks the time-reversal symmetry. The Hamiltonian belongs to the class D in the tenfold AZ symmetry class classification [10].

The quasiparticle (Bogoliubov) excitation is a gapped excitation, except for $\mu = 0, \pm 4t$. At $\mu = 0, \pm 4t$, the Bogoliubov excitation forms point nodes at high symmetric momentum points. Especially, when $\mu = -4t$, the particle and the hole bands form a gapless Dirac-cone dispersion around $(k_x, k_y) = (0, 0)$,

$$\mathbb{H}(\boldsymbol{k}) \simeq \begin{pmatrix} m - t\left(k_x^2 + k_y^2\right) & 2\Delta(k_x - ik_y) \\ 2\Delta(k_x + ik_y) & -m + t\left(k_x^2 + k_y^2\right) \end{pmatrix}. \tag{6}$$

A finite $m \equiv \mu + 4t$ endows the gapless Dirac fermion with a finite gap. In the gapped phase, the bulk state is characterized by a quantized thermal Hall conductivity $\kappa_{xy} = C\pi^2 k_B^2 T/6h$ with C a quantized integer number [12]. The gapless point $m = 0$ separates the two gapped phases with the quantized number $C = 0$ ($m < 0$) and $C = -1$ ($m > 0$). The low-energy effective theory around $m \simeq 0$ and around the Γ point ($\boldsymbol{k} \simeq 0$) is described by a Dirac fermion Hamiltonian for a slowly-varying component of the Nambu field $\psi(\boldsymbol{r})$,

$$\hat{H}_0 = \int d^2\boldsymbol{x}\, \psi^\dagger(\boldsymbol{x})(v\boldsymbol{\sigma} \cdot \hat{\boldsymbol{p}} + m\sigma_3)\psi(\boldsymbol{x}), \tag{7}$$

with $\hat{\boldsymbol{p}} \equiv -i\boldsymbol{\partial} \equiv (-i\partial_x, -i\partial_y)$, $\boldsymbol{\sigma} \equiv (\sigma_1, \sigma_2)$, a uniform mass term m and a Dirac fermion's velocity $v \equiv 2\Delta$. The Dirac fermion Hamiltonian generally describes a phase transition between two gapped phases with their topological numbers being different from each other by one.

The gapped phase with $C = 0$ stands for a topologically trivial superconductor (SC) phase. On increasing the disorder strength W in the trivial SC phase, the band gap gets narrower, which eventually leads to localized zero-energy quasiparticle Majorana states in the trivial SC phase [32]. The focus of the paper is whether the zero-energy quasiparticle Majorana states are either ballistic, diffusive or localized in space. Thus, we call such trivial SC phase with localized zero-energy states as a conventional Anderson insulator (AI) phase. In fact, a recent numerical study on a 2D class-D lattice model demonstrates that the trivial SC phase with weak disorder can be continuously connected to a phase of the highly localized zero-energy Majorana states by very strong disorders [32]. Here, "continuously connected" means that the two phases are not separated by either quantum critical point (line or surface) or delocalized phase in a generic phase diagram of the class-D symmetry.

The gapped phase with $C = \pm 1$ represents a topological superconductor (TS) phase. Whether the positive m corresponds to TS or AI phase depends on a global topology of the BdG Hamiltonian in the clean limit; the Dirac fermion Hamiltonian can only tell that when the positive m corresponds to TS with $C = -1$ (AI) phase, then the negative m corresponds to AI (TS with $C = +1$) phase. For simplicity, we call the positive (negative) m side to be in the TS (AI) phase throughout this paper.

The chemical-potential type disorder in the tight-binding Hamiltonian Eq. (4) results in a Dirac-mass-type disorder potential in the Dirac Hamiltonian,

$$\hat{H}[\{V_3(\boldsymbol{r})\}] = \hat{H}_0 + \int d^2\boldsymbol{x} V_3(\boldsymbol{x}) \psi^\dagger(\boldsymbol{x}) \sigma_3 \psi(\boldsymbol{x}). \tag{8}$$

$V_3(\boldsymbol{x})$ is the Dirac-mass-type disorder potential, which is short-ranged and obeys the Gaussian distribution under a quenched average $\langle \cdots \rangle_{\rm dis}$, i.e., $\langle V_3(\boldsymbol{r}) \rangle_{\rm dis} = 0$, $\langle V_3(\boldsymbol{x}) V_3(\boldsymbol{x}') \rangle_{\rm dis} = \Delta_3 \delta^2(\boldsymbol{x} - \boldsymbol{x}')$. The disordered Dirac Hamiltonian keeps the particle-hole symmetry.

III. FIELD THEORY FOR THE RANDOM-MASS DIRAC FERMION

Disorder-averaged Green functions for the disordered single-particle Dirac Hamiltonian can be systematically treated by a replica method [53,54]. In the replica method, R-numbers of the identical free Dirac fermion Hamiltonians of $\hat{H}_0$ are replicated together with an elastic-scattering interaction among the replicated Dirac fermions,

$$\begin{aligned} S_{\rm eff} = & \int d\tau \int d^2\boldsymbol{x}\, \psi_\alpha^\dagger(\boldsymbol{x}, \tau)(\partial_\tau + v\boldsymbol{\sigma} \cdot \hat{\boldsymbol{p}} + m\sigma_3)\psi_\alpha(\boldsymbol{r}, \tau) \\ & - \frac{\Delta_3}{2} \int d\tau d\tau' \int d^2\boldsymbol{x} (\psi_\alpha^\dagger \sigma_3 \psi_\alpha)_{\boldsymbol{x},\tau} (\psi_\beta^\dagger \sigma_3 \psi_\beta)_{\boldsymbol{x},\tau'}, \end{aligned} \tag{9}$$

with replica indices $\alpha, \beta = 1, \cdots R$. Here the summation over the replica indices are omitted in Eq. (9), and will be omitted in the following unless mentioned otherwise. The disorder-averaged connected Green functions for the disordered single-particle Hamiltonian are equivalent to Green functions for the replicated effective action $S_{\rm eff}$ in a zero-replica limit ($R \to 0$); e.g., see Appendix A.

Based on the equivalence, we will argue renormalizability of $S_{\rm eff}$ around the gapless point ($m = 0$) and the clean limit ($\Delta_3 = 0$) in the replica limit ($R \to 0$). To put it generally, we

consider the replica action $S_{\rm eff}$ in general spatial dimensions. The d-dimensional action at the gapless point takes a form of

$$S_{\rm eff} = S_0 + S_I,$$

$$S_0 = \int d^d\boldsymbol{x} d\tau\, \psi_\alpha^\dagger(\boldsymbol{x},\tau)\,(\partial_\tau - iv\boldsymbol{\gamma}\cdot\boldsymbol{\nabla})\psi_\alpha(\boldsymbol{x},\tau), \tag{10}$$

$$S_I = -\frac{\Delta_3}{2}\int d^d\boldsymbol{x} d\tau d\tau' (\psi_\alpha^\dagger\hat{\gamma}\psi_\alpha)_{\boldsymbol{x},\tau}(\psi_\beta^\dagger\hat{\gamma}\psi_\beta)_{\boldsymbol{x},\tau'}, \tag{11}$$

with $\boldsymbol{\nabla} \equiv (\partial_1, \partial_2, \cdots, \partial_d)$, where $\boldsymbol{\gamma} \equiv (\gamma_i)$ $(i = 1, \cdots, d)$ is a d-components vector of matrices that generate a d-dimensional Clifford algebra satisfying the anticommutation relations $\{\gamma_i, \gamma_j\} = 2\delta_{ij}$ $(i, j = 1, \cdots, d)$ and $\gamma_0 = I$. $\hat{\gamma}$ is a generalization of the 2D Pauli matrix σ_3 into the d-dimensions, with the anticommunication relation $\{\gamma_i, \hat{\gamma}\} = 0$.

A. Renormalizability

The d-dimensional effective field theory around the clean-limit fixed point has the two spatial dimensions ($d = 2$) as its upper critical dimension [33]. In a unit of an inverse length (scaling of momentum), dimensions of coordinate and derivatives are given by $\dim[x] = \dim[\tau] = -1$ and $\dim[\partial_\tau] = \dim[\partial_x] = 1$. To evaluate a tree-level scaling dimension of the disorder strength, we take the action $S_{\rm eff}$ to be dimensionless, $\dim[S_{\rm eff}] = 0$. In a perturbative renormalization group analysis around the clean-limit fixed point, the velocity and the coefficient in front of ∂_τ in S_0 are chosen to be marginal at the tree-level: $\dim[v] = 0$. Then, a dimension of the field operator is given by $\dim[\psi] = d/2$. The disorder strength has a dimension $\dim[\Delta_3] = 2 - d$ from S_I in Eq. (11). Thus, the disorder strength is marginal, irrelevant and relevant at the tree level in $d = 2$, $d > 2$ and $d < 2$, respectively [55].

The Green functions of the action $S_{\rm eff}$ may have ultraviolet (UV) divergences. The UV divergences can be renormalizable, nonrenormalizable and super-renormalizable in $d = 2$, $d > 2$, and $d < 2$, respectively. To explain the UV divergences in the Green functions and their renormalizability in general d dimensions, let us put the action $S_{\rm eff} = S_0 + S_I$ in the momentum-frequency space,

$$S_0 = \int_k \psi_\alpha^\dagger(\boldsymbol{k},\omega)\,(-i\omega + v\boldsymbol{\gamma}\cdot\boldsymbol{k})\psi_\alpha(\boldsymbol{k},\omega), \tag{12}$$

$$S_I = -\frac{\Delta_3}{2}\int_{\omega_1,\omega_2}\int_{\boldsymbol{k}_1,\boldsymbol{k}_2,\boldsymbol{k}_3} \psi_\alpha^\dagger(\boldsymbol{k}_1,\omega_1)\hat{\gamma}\psi_\alpha(\boldsymbol{k}_3,\omega_1) \times \psi_\beta^\dagger(\boldsymbol{k}_2,\omega_2)\hat{\gamma}\psi_\beta(\boldsymbol{k}_1+\boldsymbol{k}_2-\boldsymbol{k}_3,\omega_2), \tag{13}$$

with momentum and frequency integrals,

$$\int_k \equiv \int_{\boldsymbol{k}}\int_\omega, \quad \int_\omega = \int_{-\infty}^{+\infty}\frac{d\omega}{2\pi}, \quad \int_{\boldsymbol{k}} = \int_{|\boldsymbol{k}|<\Lambda}\frac{d^d\boldsymbol{k}}{(2\pi)^d}. \tag{14}$$

Here Λ is a UV momentum cutoff. The interaction in Eq. (13) does not exchange energy (frequency) or replica index.

Disorder-averaged $2n$-point connected Green functions in the disordered single-particle Hamiltonian are identical to $2n$-point Green functions for the replica action $S_{\rm eff}$ in the zero replica limit; see Eqs. (A5) and (A7) in Appendix A. We thus consider the renormalization of the $2n$-point Green functions of $S_{\rm eff}$ in the limit of $R \to 0$. In the momentum-frequency space, they are defined as follows:

$$(2\pi)^{d+1}\delta^{(d)}(\boldsymbol{k}-\boldsymbol{k}')\delta(\omega-\omega')G_\alpha^{(2)}(\boldsymbol{k},\omega) \equiv \frac{1}{Z_{\rm eff}}\int D\psi_\gamma^\dagger D\psi_\gamma\, \psi_\alpha(\boldsymbol{k},\omega)\psi_\alpha^\dagger(\boldsymbol{k}',\omega')\, e^{-S_{\rm eff}}, \tag{15}$$

$$(2\pi)^{d+2}\delta^{(d)}(\boldsymbol{k}_1+\boldsymbol{k}_2-\boldsymbol{k}_3-\boldsymbol{k}_4)\delta(\omega_1-\omega_4)\delta(\omega_2-\omega_3)G_{\alpha\beta}^{(4)}(\boldsymbol{k}_1,\boldsymbol{k}_2,\boldsymbol{k}_3;\omega_1,\omega_2) \equiv \frac{1}{Z_{\rm eff}}\int D\psi_\gamma^\dagger D\psi_\gamma e^{-S_{\rm eff}}\psi_\alpha(\boldsymbol{k}_1,\omega_1)\psi_\beta(\boldsymbol{k}_2,\omega_2)\psi_\beta^\dagger(\boldsymbol{k}_3,\omega_3)\psi_\alpha^\dagger(\boldsymbol{k}_4,\omega_4), \tag{16}$$

with

$$Z_{\rm eff} \equiv \int D\psi_\alpha^\dagger D\psi_\alpha e^{-S_{\rm eff}}. \tag{17}$$

According to the standard Dyson-Feynman perturbation theory, the Green functions are given by amputated one-particle irreducible (1PI) parts of the connected Green's functions (vertex functions) [53,55,56]. The two-point and four-point vertex functions, $\Gamma_\alpha^{(2)}$ and $\Gamma_{\alpha\beta}^{(4)}$, are related to the respective Green functions,

$$G_\alpha^{(2)}(\boldsymbol{k},\omega)\Gamma_\alpha^{(2)}(\boldsymbol{k},\omega) = 1, \tag{18}$$

$$G_{\alpha\beta}^{(4)}(\boldsymbol{k}_1,\boldsymbol{k}_2,\boldsymbol{k}_3;\omega_1,\omega_2) = G_\alpha(\boldsymbol{k}_1,\omega_1)G_\beta(\boldsymbol{k}_2,\omega_2)G_\beta(\boldsymbol{k}_3,\omega_2)G_\alpha(\boldsymbol{k}_1+\boldsymbol{k}_2-\boldsymbol{k}_3,\omega_1)\Gamma_{\alpha\beta}^{(4)}(\boldsymbol{k}_1,\boldsymbol{k}_2,\boldsymbol{k}_3;\omega_1,\omega_2) + G_\alpha^{(2)}(\boldsymbol{k}_1,\omega_1)G_\beta^{(2)}(\boldsymbol{k}_2,\omega_2)(2\pi)^d\delta^{(d)}(\boldsymbol{k}_2-\boldsymbol{k}_3). \tag{19}$$

Similarly, higher-order $2n$-point vertex functions can be defined from the $2n$-point connected Green functions [53,55,56]. Note that those 1PI parts with closed internal fermion loops vanish in the limit of the zero replica, as every loop gives a factor R. Thus, frequencies and replica indices of all the internal fermion lines in the 1PI parts are fixed by those of external fermion lines. The 1PI parts are given only by integrals over the internal momenta that depend on the UV momentum cutoff Λ.

The $2n$-point vertex functions $\Gamma_{\alpha_1\cdots\alpha_n}^{(2n)}$ could diverge when the UV momentum cutoff Λ is taken infinitely large. To evaluate how $\Gamma^{(2n)}$ with $n \equiv N_F/2$ number of external fermion lines diverges in the limit of the large Λ, let us suppose that an amputated Feynman diagram with the N_F external fermion

points has integrals over L-number of internal d-dimensional momenta. The integrand is a product among V_F number of internal fermion lines and V number of the fermion's quartic couplings (vertices). From dimensional power counting [55,56], superficial degree of the UV divergence M of the amputated diagram is given by $M = dL - V_F$. Each vertex of the quartic coupling connects four fermion lines and each fermion line attaches to two vertices or external points. Thus, the total number of internal and external fermion lines of an unamputated Feynman diagrams is given by $V_F + N_F = 2V + N_F/2$. Each vertex with four fermion lines imposes a momentum conservation onto four momenta of the four fermion lines. Besides, the total sum of the external momenta is zero. Thus, $L = V_F - (V - 1)$. Combing them together, we obtain M in terms of N_F and V as follows:

$$M = d - \frac{d-1}{2}N_F + (d-2)V. \tag{20}$$

This shows that the system is renormalizable, nonrenormalizable, and super-renormalizable at $d = 2$, $d > 2$, and $d < 2$, respectively [55,56].

At $d = 2$, the superficial degree of the UV divergence of the amputated 1PI parts only depends on the number of the external fermion points, i.e., $M = 2 - N_F/2$. Two-point ($N_F = 2$) and four-point ($N_F = 4$) vertex functions in Eqs. (18) and (19) have potentially UV divergences in the large Λ limit, while $\Gamma^{(N_F)}$ ($N_F \geqslant 6$) has no UV divergence. The dimensional counting shows that in the two-point vertex function $\Gamma^{(2)}$, the coefficient of σ_3 has a linear divergence in Λ, while those coefficients of ω and $\boldsymbol{k}$ have the logarithmic divergence in Λ. Note that because of the particle-hole symmetry, $\Gamma^{(2)}$ has no σ_0 term that is linear in Λ. Thus, the most general form of the divergences in the two-point vertex is given by

$$\begin{aligned}\Gamma^{(2)}_{\alpha}(\boldsymbol{k},\omega) = (\cdots)\cdot\Lambda\sigma_3 + (\cdots)\cdot\ln\Lambda\cdot(-i\omega)\\ + (\cdots)\cdot\ln\Lambda\cdot(v\boldsymbol{\sigma}\cdot\boldsymbol{k}).\end{aligned} \tag{21}$$

The linear divergence in Eq. (21) can be absorbed into a shift of the uniform mass, so that the theory remains massless. In practice, the Λ linear term does not appear in the following perturbative renormalization calculation (see Sec. IV). The logarithmic UV divergences in the coefficients of ω and $\boldsymbol{k}$ can be absorbed into renormalizations of field operator amplitude and the single-particle energy (frequency) ω. The four-point vertex function is dimensionless and shows the logarithmic divergence in Λ,

$$\begin{aligned}\Gamma^{(4)}_{\alpha\beta}(\cdots) = (\cdots)\cdot\ln\Lambda\cdot\sigma_3\otimes\sigma_3\\ + (\cdots)\cdot\ln\Lambda\cdot(\text{other `}\otimes\text{ tensor products'})\\ + \mathcal{O}(\omega,k).\end{aligned} \tag{22}$$

Under the particle-hole symmetry, the logarithmic UV divergence is allowed to take a tensor form of $\sigma_3\otimes\sigma_3$ as well as other tensor forms, e.g., $\sigma_0\otimes\sigma_0$, $\sigma_j\otimes\sigma_j$ with $j = 1, 2$. The logarithmic divergence with $\sigma_3\otimes\sigma_3$ can be absorbed into a renormalization of the disorder strength Δ_3. When the logarithmic divergence appears in coefficients of the other tensor forms, one should also include such tensor forms of bare interactions into the original action S_{eff} to make the theory to be renormalizable. In the following two-loop calculation, we will see that only the coefficient of $\sigma_3\otimes\sigma_3$ has the UV divergence, while the coefficients of the other forms have no UV divergence. When all the UV divergences in the vertex functions are absorbed into the renormalizations of field operator amplitude, the single-particle energy ω, disorder strength Δ_3 and the uniform mass m, the effective field theory is renormalizable.

IV. RENORMALIZATION

In the previous section, we introduced three kinds of the logarithmic UV divergences in vertex functions $\Gamma^{(N_F)}$ ($N_F = 2, 4$), Eqs. (21) and (22). In this section, we include them into the renormalization of the field operator strength Z_2 with $\psi \equiv \sqrt{Z_2}\phi$, the renormalization of single-particle energy (frequency) ω and renormalization of the effective interaction Δ_3. In practice, we use the dimensional regularization by putting spatial dimensions into $d = 2 - \epsilon$, where $\ln\Lambda$ in $d = 2$ becomes $1/\epsilon$ in small ϵ [34,55,57–59]. In the following, we will see that $\Gamma^{(2)}$ and $\Gamma^{(4)}$ in $d = 2 - \epsilon$ have $1/\epsilon$ divergent terms and we shall include them into the renormalizations of the field strength, the single-particle energy and the interaction strength.

To this end, we use a minimal subtraction method [55,59] and separate the action in Eqs. (11) and (12) into an effective action S_E and counterterm part S_C,

$$\begin{aligned}S_{\text{eff}} &= S_E + S_C,\\ S_E &= \int_{\boldsymbol{k},\omega}\phi^\dagger_\alpha(\boldsymbol{k},\omega)\,(-i\Omega + v\boldsymbol{\gamma}\cdot\boldsymbol{k})\phi_\alpha(\boldsymbol{k},\omega)\\ &\quad - \frac{\Omega^\epsilon\kappa}{2}\int d\tau d\tau'\int d^d\boldsymbol{x}(\phi^\dagger_\alpha\hat{\gamma}\phi_\alpha)_{\boldsymbol{x},\tau}(\phi^\dagger_\beta\hat{\gamma}\phi_\beta)_{\boldsymbol{x},\tau'},\end{aligned} \tag{23}$$

$$\begin{aligned}S_C &= \int_{\boldsymbol{k},\omega}\phi^\dagger_\alpha(\boldsymbol{k},\omega)\,(-i\delta\Omega + \delta_2 v\boldsymbol{\gamma}\cdot\boldsymbol{k})\phi_\alpha(\boldsymbol{k},\omega)\\ &\quad - \frac{\Omega^\epsilon\delta\kappa}{2}\int d\tau d\tau'\int d^d\boldsymbol{x}(\phi^\dagger_\alpha\hat{\gamma}\phi_\alpha)_{\boldsymbol{x},\tau}(\phi^\dagger_\beta\hat{\gamma}\phi_\beta)_{\boldsymbol{x},\tau'}.\end{aligned} \tag{24}$$

Here ϕ is a renormalized field and it is related with the bare field ψ by a field renormalization $\sqrt{Z_2}$,

$$\psi \equiv \sqrt{Z_2}\phi, \quad Z_2 \equiv 1 + \delta_2, \tag{25}$$

with a field counterterm δ_2. Ω and $\delta\Omega$ are the renormalized single-particle energy and its counterterm,

$$\Omega + \delta\Omega = Z_2\omega. \tag{26}$$

κ and $\delta\kappa$ are renormalized *dimensionless* interaction strength and its counterterm. Since Δ_3 has a scaling dimension of $2 - d$: $\dim[\Delta_3] = \epsilon$, we normalize Δ_3 by Ω^ϵ to have dimensionless κ,

$$\Omega^\epsilon(\kappa + \delta\kappa) = Z_2^2\Delta_3. \tag{27}$$

In this renormalization scheme, the renormalized single-particle energy Ω plays a role of a renormalization group (RG) scale, where all the physical quantities are normalized by a proper power of Ω. Taking Ω to be finite, we can also control infrared divergences that could appear in momentum integrals for self-energy and the vertex function. The renormalization of the single-particle energy results in an anisotropy in space

and time [54], leading to a nontrivial dynamical exponent around a nontrivial fixed point [see Eq. (39)].

The primary objective of the renormalization is to make the two-point and four-point vertex functions of the *renormalized* field to be free from the UV divergences as functions of the renormalized quantities, κ and Ω. The vertex functions and Green functions of the renormalized field (let us call them renormalized vertex and Green functions, respectively) are defined through the same equations as Eqs. (15), (16), (18), and (19) with the same action and partition function as $S_{\rm eff}$ and $Z_{\rm eff}$ and with the bare fields ψ being replaced by the renormalized field ϕ, e.g.,

$$\overline{G}_\alpha(\boldsymbol{k},\Omega)\overline{\Gamma}_\alpha(\boldsymbol{k},\Omega)=1, \tag{28}$$

$$\begin{aligned}&(2\pi)^{d+1}\delta^{(d)}(\boldsymbol{k}-\boldsymbol{k}')\delta(\omega-\omega')\overline{G}^{(2)}_\alpha(\boldsymbol{k},\Omega)\\&\quad\equiv\frac{1}{Z_{\rm eff}}\int D\psi^\dagger_\gamma D\psi_\gamma\,\phi_\alpha(\boldsymbol{k},\omega)\phi^\dagger_\alpha(\boldsymbol{k}',\omega')\,e^{-S_{\rm eff}}.\end{aligned} \tag{29}$$

Here the renormalized frequency Ω in the left-hand sides and bare frequency ω in the right-hand side of Eq. (29) are related to each other by Eq. (26). The UV divergent terms in the vertex functions of the bare field can be then absorbed into the counterterms, δ_2, $\delta\kappa$, and $\delta\Omega$, in such a way that the renormalized vertex functions have no UV divergence as functions of renormalized quantities κ and Ω.

To this end, κ in Eq. (23) and S_C in Eq. (24) are treated perturbatively, and two-point and four-point renormalized vertex functions are calculated in terms of the standard perturbation theory. The $1/\epsilon$ divergent terms and the counterterms are set to cancel each other in the renormalized vertex functions at every order in the perturbation. In the perturbative expansion, the zeroth-order renormalized Green function is given by the first term in Eq. (23):

$$\overline{G}_0(\boldsymbol{p},\Omega)=\frac{1}{-i\Omega+v\boldsymbol{\gamma}\cdot\boldsymbol{p}}=\frac{i\Omega+v\boldsymbol{\gamma}\cdot\boldsymbol{p}}{\Omega^2+v^2\boldsymbol{p}^2}. \tag{30}$$

The velocity v is free from the renormalization in this RG scheme. We henceforth set $v=1$ for simplicity.

To cancel $1/\epsilon$ divergent terms by the counterterms in the two-point renormalized vertex function, we require the two-point renormalized vertex function as a function of κ and Ω to be on the order of $\mathcal{O}(\epsilon^0)$ in the small ϵ limit,

$$\begin{aligned}\overline{\Gamma}^{(2)}_\alpha(\boldsymbol{k},\Omega)&\equiv-i(\Omega+\delta\Omega)+(1+\delta_2)\boldsymbol{\gamma}\cdot\boldsymbol{k}-\overline{\Sigma}(\boldsymbol{k},\Omega)\\&=-i\Omega+\boldsymbol{\gamma}\cdot\boldsymbol{k}+\mathcal{O}(1).\end{aligned} \tag{31}$$

To cancel $1/\epsilon$ divergent terms by the counterterm in the four-point renormalized vertex function, we require the four-point renormalized vertex function at $\Omega_1=\Omega_2=\Omega$ and at $\boldsymbol{k}_1=\boldsymbol{k}_2=\boldsymbol{k}_3=0$ to be finite as a function of κ and Ω in the small ϵ limit,

$$\begin{aligned}&\overline{\Gamma}^{(4)}_{\alpha\beta}(\boldsymbol{k}_1,\boldsymbol{k}_2,\boldsymbol{k}_3;\Omega_1,\Omega_2)|_{\boldsymbol{k}_i=0,\Omega_1=\Omega_2=\Omega}\\&\quad\equiv\Omega^\epsilon(\kappa+\delta\kappa)\hat{\gamma}\otimes\hat{\gamma}+\overline{\Gamma}^{(4),\prime}_{\alpha\beta}(\boldsymbol{0},\boldsymbol{0},\boldsymbol{0};\Omega,\Omega)\\&\quad=\Omega^\epsilon\kappa\,\hat{\gamma}\otimes\hat{\gamma}+\mathcal{O}(1).\end{aligned} \tag{32}$$

Note that an external single-particle energy Ω is kept finite, so that the integrals in the right-hand sides are free from any infrared divergence associated with the momentum integrals.

Based on Eqs. (31) and (32), the counterterms, δ_2, $\delta\kappa$, and $\delta\Omega$ in Eqs. (31) and (32), are set to cancel the divergent contribution (in power of $1/\epsilon$) in the self energy $\overline{\Sigma}$ and four-point vertex function $\overline{\Gamma}^{(4),\prime}_{\alpha\beta}$ order by order in κ. Being dimensionless, δ_2, $\delta\kappa$ and $\delta\Omega/\Omega$ thus obtained are given as functions only of the dimensionless disorder strength κ [see, for example, Eqs. (33), (34), (35), (36), and (37)]. The bare coupling constant Δ_3 and the bare single-particle energy ω are given by κ and Ω through Eqs. (25), (27), and (26).

For simplicity of the following notation, we rescale the dimensionless disorder strength κ by the spherical integral of d-dimensional momentum [59,60], to have another dimensionless disorder strength g,

$$g=2C_d\kappa,\quad C_d\equiv\int\frac{dS_d}{(2\pi)^d}=\frac{2^{1-d}\pi^{-d/2}}{\Gamma(d/2)}. \tag{33}$$

We use g instead of κ throughout the remaining part of the paper.

The vertex functions of $S_{\rm eff}$ are renormalized at a finite single-particle energy Ω through Eqs. (31) and (32), where high-energy (short-ranged) degrees of freedom in the bare vertex functions are renormalized into the counterterms. The bare disorder strength Δ_3 and bare single-particle energy ω are given as functions of renormalized disorder strength g and renormalized single-particle energy (RG scale) Ω,

$$\Delta_3=\Omega^\epsilon Z_2^{-2}(\kappa+\delta\kappa)\equiv\frac{\Omega^\epsilon}{2C_d}Z_g g, \tag{34}$$

$$\omega=Z_2^{-1}(\Omega+\delta\Omega)\equiv Z_\omega\Omega, \tag{35}$$

$$Z_2=1+\delta_2. \tag{36}$$

The divergent contributions in the bare vertex functions in the small ϵ limit are included in the three renormalization constants, $Z_\mu=Z_2,Z_\omega,Z_g$ ($\mu=2,\omega,g$). Being dimensionless, these constants must be polynomials in the dimensionless disorder strength g. Namely, they generally take the following forms,

$$Z_\mu(\epsilon,g)\equiv1+\delta_\mu=1+\sum_{n=1}^{m}\frac{a_{n,\mu}(g)}{\epsilon^n}, \tag{37}$$

with $\mu=2,\omega,g$. Here $a_{n,\mu}(g)$ is an mth order polynomial of g in the m-loop perturbative RG calculation.

The renormalized vertex functions in the small Ω limit determine ground-state nature of the action $S_{\rm eff}$ [55,59]. When Ω goes to the zero with a fixed Δ_3, g changes according to Eq. (34). Thereby, a limiting value of the renormalized disorder strength g in the small Ω limit determines the ground state phase diagram of the action $S_{\rm eff}$. To determine how g changes in the small Ω limit, let us take an Ω derivative of Eq. (34) with a fixed Δ_3,

$$\begin{aligned}0\equiv\Omega\frac{\partial\Delta_3}{\partial\Omega}&=\Omega^\epsilon gZ_g\Big(\epsilon+\frac{\Omega}{g}\frac{\partial g}{\partial\Omega}+\frac{\Omega}{Z_g}\frac{\partial Z_g}{\partial\Omega}\Big)\\&=\Omega^\epsilon gZ_g\bigg[\epsilon+\frac{\partial\ln g}{\partial\ln\Omega}\Big(1+\frac{d\ln Z_g}{d\ln g}\Big)\bigg].\end{aligned}$$

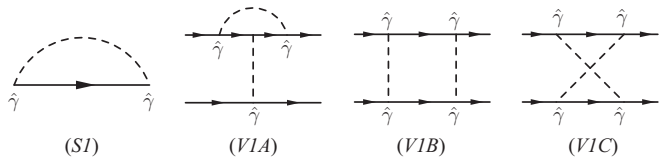

FIG. 2. One-loop diagrams: ($S1$) self-energy; ($V1$) four-point vertex function. Solid line stands for the zeroth order renormalized Green function given in Eq. (30). Dotted line stands for the effective interaction with κ in S_E.

The derivative gives out a β function of the coupling constant g, β_g, that tells how g changes in the small Ω limit,

$$\frac{\partial g}{\partial l} = -\beta_g = \epsilon g\Big(1 + g\frac{d\ln Z_g}{dg}\Big)^{-1}, \tag{38}$$

with an RG parameter $l \equiv -\ln\Omega$. The small Ω limit corresponds to the large l limit. Z_g is a polynomial function of g [Eq. (37)] and so is the β function. In the next section, we will calculate the β function up to the two-loop level (the third order in g). In Sec. VI, we deduce the β function up to the four-loop level (the fifth order in g) using a correspondence between the random Dirac fermion Hamiltonian model and an SU(N) Gross-Neveu model.

The renormalized single-particle energy Ω plays a role of the scale parameter in this RG scheme [54,55,59]. According to the renormalization condition Eq. (31), Ω has the same scaling as the momentum or inverse of the length scale in the long wavelength limit. When Ω goes to zero with a fixed Δ_3, the bare single-particle energy ω changes according to Eqs. (34) and (35), e.g., ω also goes to zero. According to the definitions of the renormalized Green functions, e.g., Eq. (29), the bare frequency ω thus changed is dual to temporal variables in the renormalized Green functions. Thus, a scaling of the bare frequency with respect to the RG scale Ω under a fixed Δ_3 determines how a characteristic time is scaled by a characteristic length in the infrared (IR) regime. To be more specific, we can define the dynamical exponent z [59] as a derivative of $\ln\omega$ with respect to $\ln\Omega$ with a fixed Δ_3,

$$z \equiv \frac{\partial\ln\omega}{\partial\ln\Omega} = 1 + \frac{\partial\ln Z_\omega}{\partial\ln\Omega} = 1 + \beta_g\frac{d\ln Z_\omega}{dg}, \tag{39}$$

where Eq. (35) was used from the second equality in the right-hand side. Note that Z_ω is a polynomial function of g [Eq. (37)] and so is the dynamical exponent. In the next section, we will calculate the dynamical exponent up to the two-loop level (the second order in g).

A. One-loop renormalization

We first calculate the one-loop renormalization. One-loop diagrams to the right-hand sides of Eqs. (31) and (32) are shown in Fig. 2. A diagram $[S1]$ gives the one-loop contribution to the self-energy part $\overline{\Sigma}(\boldsymbol{k}, \Omega)$ in Eq. (31),

$$[S1] = \kappa\Omega^\epsilon\hat{\gamma}\int_p \overline{G}_0(\boldsymbol{p})\hat{\gamma} = \big(i\Omega\big)\frac{g}{2\epsilon}, \tag{40}$$

with the zeroth order renormalized Green function $\overline{G}_0(\boldsymbol{p})$ defined in Eq. (30). Since the single-particle energies in any internal fermion lines in Feynman diagrams are always fixed to be Ω in the RG conditions, Eqs. (31) and (32), we omit the argument Ω in $\overline{G}_0(\boldsymbol{p}, \Omega)$ and simplify it by $\overline{G}_0(\boldsymbol{p})$. Equation (40) has no linear term in $\boldsymbol{\gamma}\cdot\boldsymbol{p}$. Thus, $\delta_2 = 0$ at the one-loop level. The one-loop contributions to the four-point vertex function are shown in the three diagrams, $[V1A]$, $[V1B]$, and $[V1C]$. The diagram $[V1A]$ takes a tensor form of $\hat{\gamma}\otimes\hat{\gamma}$,

$$\begin{aligned}[V1A] &= \kappa^2\Omega^{2\epsilon}\int_p \overline{G}_0(-\boldsymbol{p})\overline{G}_0(\boldsymbol{p})\hat{\gamma}\otimes\hat{\gamma} \\ &= -\kappa^2\Omega^{2\epsilon}\int_p \frac{1}{\Omega^2+p^2}\hat{\gamma}\otimes\hat{\gamma} = -\frac{\Omega^\epsilon}{2C_d}\frac{g^2}{2\epsilon}\hat{\gamma}\otimes\hat{\gamma}.\end{aligned} \tag{41}$$

The diagram $[V1B]$ and $[V1C]$ take tensor forms of $\gamma_i\otimes\gamma_j$ ($i, j = 0, 1, \cdots, d$), respectively:

$$\begin{aligned}[V1B] &= \kappa^2\Omega^{2\epsilon}\int_p \frac{i\Omega - \boldsymbol{\gamma}\cdot\boldsymbol{p}}{\Omega^2+p^2}\otimes\frac{i\Omega+\boldsymbol{\gamma}\cdot\boldsymbol{p}}{\Omega^2+p^2}, \\ [V1C] &= \kappa^2\Omega^{2\epsilon}\int_p \frac{i\Omega - \boldsymbol{\gamma}\cdot\boldsymbol{p}}{\Omega^2+p^2}\otimes\frac{i\Omega-\boldsymbol{\gamma}\cdot\boldsymbol{p}}{\Omega^2+p^2}.\end{aligned}$$

However, a sum of these two diagrams is on the order of one in the limit of $\epsilon\to 0$:

$$\begin{aligned}[V1B]+[V1C] &= \kappa^2\Omega^{2\epsilon}\int_p \frac{i\Omega-\boldsymbol{\gamma}\cdot\boldsymbol{p}}{\Omega^2+p^2}\otimes\frac{2i\Omega}{\Omega^2+p^2}, \\ &= \kappa^2\Omega^{2\epsilon}\int_p \frac{-2\Omega^2}{\Omega^2+p^2}\frac{1}{\Omega^2+p^2}\gamma_0\otimes\gamma_0 = \mathcal{O}(1).\end{aligned} \tag{42}$$

Thus, at the one-loop level, no new vertex form other than $\hat{\gamma}\otimes\hat{\gamma}$ is generated with the divergence.

The one-loop counterterms in Eqs. (31) and (32) should cancel the $1/\epsilon$ divergent terms in the self-energy Eq. (40) and the vertex function Eqs. (41) and (42),

$$\begin{aligned}-i\delta^{(1)}\Omega - [S1] &= \mathcal{O}(1), \\ \Omega^\epsilon\delta^{(1)}\kappa\hat{\gamma}\otimes\hat{\gamma} + 2[VIA] + [V1B] + [V1C] &= \mathcal{O}(1),\end{aligned}$$

with a proper symmetry factor for $[V1A]$. We obtain the one-loop counterterms:

$$\delta^{(1)}\Omega = -\Omega\frac{g}{2\epsilon}, \quad \Omega^\epsilon\delta^{(1)}\kappa = \frac{\Omega^\epsilon}{2C_d}\frac{g^2}{\epsilon}. \tag{43}$$

Here $\delta^{(m)}\kappa$, $\delta^{(m)}\Omega$, and $\delta_2^{(m)}$ stand for the m-loop contributions to the counterterms, $\delta\kappa$, $\delta\Omega$, and δ_2, respectively:

$$\delta\Omega \equiv \sum_{m=1}^{\infty}\delta^{(m)}\Omega,\ \delta\kappa \equiv \sum_{m=1}^{\infty}\delta^{(m)}\kappa,\ \delta_2 \equiv \sum_{m=1}^{\infty}\delta_2^{(m)}. \tag{44}$$

B. Two-loop renormalization

We now proceed to the two-loop renormalization. The two-loop self-energy diagrams are shown in Fig. 3. Diagrams $[S2A]$, $[S2a]$, and $[S2b]$ are linear in $i\Omega$ and they do not have linear terms in $\boldsymbol{\gamma}\cdot\boldsymbol{k}$. Diagram $[S2B]$ has both linear term in $i\Omega$

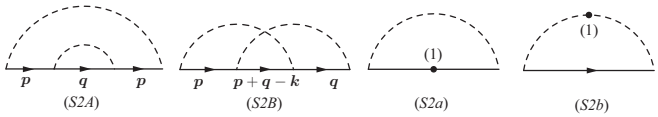

FIG. 3. Two-loop self-energy diagrams. Black circle on the solid line with (1) stands for $-i\delta^{(1)}\Omega + \delta_2^{(1)} v\boldsymbol{\gamma}\cdot\boldsymbol{k}$ in S_C where $\delta^{(1)}$ is given by Eq. (43) and $\delta_2^{(1)} = 0$. Black circle on the dotted line with (1) stands for $\delta^{(1)}\kappa$ in S_C. $\delta^{(1)}\kappa$ is given by Eq. (43).

and linear term in $\boldsymbol{\gamma}\cdot\boldsymbol{k}$. Diagrams $[S2A]$ and $[S2B]$ at $\boldsymbol{k}=0$ are given by

$$[S2A] = \kappa^2\Omega^{2\epsilon}\int_{p,q}\overline{G}_0(-p)\overline{G}_0(q)\overline{G}_0(-p)$$
$$= \big(i\Omega\big)\frac{g^2}{4\epsilon^2}\big(1-\epsilon\big) + \mathcal{O}(1), \tag{45}$$
$$[S2B](\boldsymbol{k}=0) = \kappa^2\Omega^{2\epsilon}\int_{p,q}\overline{G}_0(-p)G(p+q)\overline{G}_0(-q)$$
$$= -\,(i\Omega)\frac{3g^2}{8\epsilon^2} + \mathcal{O}(1). \tag{46}$$

The two-loop contributions with the one-loop counterterms are shown in $[S2a]$ and $[S2b]$,

$$[S2a] = \kappa\Omega^\epsilon\, i\delta^{(1)}\Omega\,\hat{\gamma}\int_p\Big(\frac{1}{-i\Omega+\boldsymbol{\gamma}\cdot\boldsymbol{p}}\Big)^2\hat{\gamma}$$
$$= -\big(i\Omega\big)\frac{g^2}{4\epsilon^2}\big(1-\epsilon\big) + \mathcal{O}(1), \tag{47}$$
$$[S2b] = \delta^{(1)}\kappa\,\Omega^\epsilon\hat{\gamma}\int_p\Big(\frac{1}{-i\Omega+\boldsymbol{\gamma}\cdot\boldsymbol{p}}\Big)\hat{\gamma}$$
$$= \big(i\Omega\big)\frac{g^2}{2\epsilon^2} + \mathcal{O}(1). \tag{48}$$

Two-loop contribution to the counterterm of the single-particle energy should cancel these $1/\epsilon$ poles in Eq. (31),

$$-i\delta^{(2)}\Omega - ([S2A] + [S2B](\boldsymbol{k}=0) + [S2a] + [S2b]) = \mathcal{O}(1). \tag{49}$$

This gives the two-loop contribution to the counterterm for the single-particle energy,

$$\delta^{(2)}\Omega = -\Omega\frac{g^2}{8\epsilon^2}. \tag{50}$$

The two-loop contribution to the field counterterm δ_2 comes from the $\boldsymbol{\gamma}\cdot\boldsymbol{k}$-linear term in the diagram $[S2B]$. The diagram $[S2B]$ for finite $\boldsymbol{k}$ is given by

$$[S2B] = \kappa^2\Omega^{2\epsilon}\int_{p,q}\overline{G}_0(-p)\overline{G}_0(p+q-k)\overline{G}_0(-q).$$

The zeroth order in the small $\boldsymbol{k}$ was already calculated and included in Eqs. (46) and (49), respectively. The $\boldsymbol{\gamma}\cdot\boldsymbol{k}$-linear term can be obtained by an expansion in $\boldsymbol{k}$ of one of the propagators:

$$\overline{G}_0(p+q-k)$$
$$= \frac{1}{\overline{G}_0^{-1}(p+q)-\boldsymbol{\gamma}\cdot\boldsymbol{k}}$$
$$= \overline{G}_0(p+q) + \overline{G}_0(p+q)(\boldsymbol{\gamma}\cdot\boldsymbol{k})\overline{G}_0(p+q) + \mathcal{O}(\boldsymbol{k}^2).$$

The linear-in-$\boldsymbol{k}$ part of $[S2B]$ is

$$[S2B](\boldsymbol{\gamma}\cdot\boldsymbol{k})$$
$$= \kappa^2\Omega^{2\epsilon}\int_{p,q}\overline{G}_0(-p)\overline{G}_0(p+q)(\boldsymbol{\gamma}\cdot\boldsymbol{k})\overline{G}_0(p+q)\overline{G}_0(-q)$$
$$= \kappa^2\Omega^{2\epsilon}\frac{1}{4\epsilon}(C_{2-\epsilon}\Omega^{-\epsilon})^2\boldsymbol{\gamma}\cdot\boldsymbol{k} + \mathcal{O}(1)$$
$$= \frac{g^2}{16\epsilon}\boldsymbol{\gamma}\cdot\boldsymbol{k} + \mathcal{O}(1). \tag{51}$$

The field counterterm δ_2 should cancel the $1/\epsilon$-pole from $[S2B](\boldsymbol{\gamma}\cdot\boldsymbol{k})$ in Eq. (31), $\delta_2\boldsymbol{\gamma}\cdot\boldsymbol{k} - [S2B](\boldsymbol{\gamma}\cdot\boldsymbol{k}) = \mathcal{O}(1)$. This gives out the two-loop contribution to the field counterterm δ_2 and the field renormalization factor Z_2 as

$$\delta_2^{(2)} = \frac{g^2}{16\epsilon}, \quad Z_2 = 1+\delta_2^{(2)} = 1+\frac{g^2}{16\epsilon}. \tag{52}$$

The two-loop contributions to the counterterm of the four-point vertex function are calculated in Appendix B. After the lengthy calculation in Appendix B, we obtain the two-loop vertex counterterm as follows:

$$\Omega^\epsilon\delta^{(2)}\kappa = \frac{\Omega^\epsilon}{2C_d}g\Big(-\frac{g^2}{8\epsilon}+\frac{g^2}{\epsilon^2}\Big). \tag{53}$$

C. Two-loop RG equations

At the two-loop level, the bare single-particle energy ω is given by a sum of the one-loop counterterm in Eq. (43) and the two-loop counterterm in Eqs. (50) together with the field renormalization factor in Eq. (52),

$$\omega = Z_2^{-1}(\Omega + \delta^{(1)}\Omega + \delta^{(2)}\Omega)$$
$$= \Big(1-\frac{g}{2\epsilon}-\frac{g^2}{8\epsilon^2}-\frac{g^2}{16\epsilon}\Big)\Omega.$$

The bare interaction is given by a sum of the one-loop counterterm in Eq. (43) and the two-loop counterterm in Eq. (53) together with the field renormalization factor in Eq. (52),

$$\Delta_3 = Z_2^{-2}(\kappa\Omega^\epsilon + \delta^{(1)}\kappa\,\Omega^\epsilon + \delta^{(2)}\kappa\,\Omega^\epsilon)$$
$$= \frac{\Omega^\epsilon}{2C_d}g\Big(1+\frac{g}{\epsilon}-\frac{g^2}{4\epsilon}+\frac{g^2}{\epsilon^2}\Big).$$

Equating these two with the renormalization constants defined in Eqs. (34) and (35), we obtain the renormalization constants as

$$Z_\omega = 1-\frac{g}{2\epsilon}-\frac{g^2}{8\epsilon^2}-\frac{g^2}{16\epsilon}, \tag{54}$$
$$Z_g = 1+\frac{g}{\epsilon}-\frac{g^2}{4\epsilon}+\frac{g^2}{\epsilon^2}. \tag{55}$$

Substituting Eq. (55) into Eq. (38) and keeping only up to the two-loop order (third order in g), we finally obtain the β function for the renormalized dimensionless disorder strength g as

$$\frac{\partial g}{\partial l} = -\beta_g = \epsilon g - g^2 + \frac{1}{2}g^3. \tag{56}$$

Substituting Eq. (54) into Eq. (39) and keeping only up to the two-loop order (second order in g), we obtain the dynamical

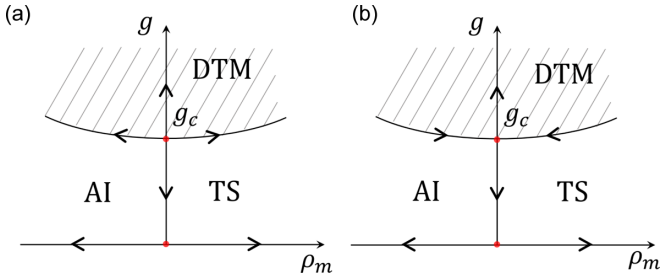

FIG. 4. Possible RG-flow phase diagram for 2D Dirac fermion with random mass. (a) uniform mass is a relevant scaling variable around the fixed point at $g = g_c$; (b) uniform mass is an irrelevant scaling variable around the fixed point at $g = g_c$.

exponent z as

$$z = 1 + \beta_g \frac{d \ln Z_\omega}{dg} = 1 + \frac{g}{2} + \frac{g^2}{8}. \tag{57}$$

D. Scaling dimension of the uniform mass

In the previous subsection, we derived the β function of the Dirac-mass type disorder strength in the absence of the uniform mass. The β function thus obtained is a function only of the renormalized disorder strength g, which has an infrared (IR) unstable fixed point at finite disorder strength ($g = g_c$) in two dimensions ($\epsilon = 0$). An important question remains; *Is the uniform mass operator relevant or irrelevant around the fixed point at $g = g_c$?* If the uniform mass m is an irrelevant scaling variable around the fixed point with the finite critical disorder strength, then the quantum criticality of DTM-AI transition as well as DTM-TS transition are controlled by the fixed point at $g = g_c$; see Fig. 4(b). If the uniform mass m is another relevant scaling variable around the fixed point with the finite critical disorder strength [Fig. 4(a)], then the quantum criticalities of these two transition lines are controlled by another saddle-point fixed point(s) at finite uniform mass, which may not be captured by $S_{\rm eff}$ studied in this paper.

To clarify the scaling property of the uniform mass, we use the same perturbative renormalization theory as in the previous section and calculate the scaling dimension of the uniform mass operator up to the two-loop order (second order in g). To this end, we treat the uniform mass operator as an external perturbation and expand the vertex functions in terms of the uniform mass m [54–56,61]. Since the uniform mass has a dimension of 1 at the clean-limit fixed point, $\dim[m] = 1$, the m-linear term of the two-point vertex function has the UV logarithmic divergence in $d = 2$. Namely, following the same line of the argument in Sec. III A, we expand the vertex functions at finite m in terms of $\boldsymbol{k}$, ω, and m in $d = 2$,

$$\Gamma^{(2)}_\alpha(\boldsymbol{k}, \omega, m) = \Gamma^{(2)}_\alpha(\boldsymbol{k}, \omega, m = 0) + (\cdots) \cdot \ln \Lambda\sigma_3 \cdot m + \mathcal{O}(m^2). \tag{58}$$

Here an m-linear term in the four-point vertex function as well as the higher-order terms in m in all the vertex functions have no UV divergence in the two dimensions. Thus, the bare theory in the presence of finite uniform mass have *one additional* logarithmic divergent term compared to the bare massless theory. The new UV divergent term can be absorbed into a renormalization of the mass m. We do this mass renormalization by using the same ϵ-expansion as in the previous section, where $\ln \Lambda$ in the two dimensions is replaced by $1/\epsilon$ in the $d = 2 - \epsilon$ dimensions.

The replicated action with the uniform mass is given by an addition of the uniform mass term into $S_{\rm eff}$ and $Z_{\rm eff}$ in Eqs. (12), (11), and (17),

$$S_{\rm eff} = \cdots + \int_{\boldsymbol{k},\omega} \psi^\dagger_\alpha(\boldsymbol{k}, \omega) m \hat{\gamma} \psi_\alpha(\boldsymbol{k}, \omega).$$

Using the same minimal subtraction method as in the previous section, we rewrite the bare field in the mass term by the renormalized field,

$$S_{\rm eff} = \cdots + \int_{\boldsymbol{k},\omega} \phi^\dagger_\alpha(\boldsymbol{k}, \omega)(1 + \delta_M) M \hat{\gamma} \phi_\alpha(\boldsymbol{k}, \omega), \tag{59}$$

where the omitted parts in $S_{\rm eff}$ are already given in Eqs. (23) and (24). Namely, we put the added mass term as

$$m \psi^\dagger_\alpha \hat{\gamma} \psi_\alpha = Z_2 Z_{\mathcal{O}}^{-1} M \phi^\dagger_\alpha \hat{\gamma} \phi_\alpha. \tag{60}$$

Here a renormalized mass M and its counterterm δ_M are related to the bare mass m as

$$m \equiv Z_{\mathcal{O}}^{-1} M, \quad Z_2 Z_{\mathcal{O}}^{-1} \equiv 1 + \delta_M, \tag{61}$$

with Z_2 the field renormalization defined in Eq. (25). The renormalized vertex functions are given as functions of $\boldsymbol{k}$, Ω and the renormalized mass M. We determine the previous counterterms ($\delta\Omega$, $\delta\kappa$, δ_2) including δ_M in such a way that the following RG conditions are satisfied by the renormalized vertex functions:

$$\overline{\Gamma}^{(2)}_\alpha(\boldsymbol{k}, \Omega, M)\big|_{M=0} = -i\Omega + \boldsymbol{\gamma} \cdot \boldsymbol{k} + \mathcal{O}(1), \tag{62}$$

$$\partial_M \overline{\Gamma}^{(2)}_\alpha(\boldsymbol{k}, \Omega, M)\big|_{\boldsymbol{k}=0,M=0} = \hat{\gamma} + \mathcal{O}(1), \tag{63}$$

$$\overline{\Gamma}^{(4)}_{\alpha\beta}(\boldsymbol{k}_1, \boldsymbol{k}_2, \boldsymbol{k}_3 : \Omega_1, \Omega_2)\big|_{\boldsymbol{k}_i=0,\Omega_i=\Omega,M=0} = \Omega^\epsilon \kappa \hat{\gamma} \otimes \hat{\gamma} + \mathcal{O}(1). \tag{64}$$

Namely, such vertex functions are free from the UV divergence as functions of renormalized single-particle energy, renormalized uniform mass and renormalized disorder strength, e.g.,

$$\overline{\Gamma}^{(2)}(\boldsymbol{k}, \Omega, M) = -i\Omega + \boldsymbol{\gamma} \cdot \boldsymbol{k} + M\hat{\gamma} + \mathcal{O}(1). \tag{65}$$

The first and the third conditions, Eqs. (62) and (64), are already satisfied by δ_2, $\delta\kappa$ and $\delta\Omega$ determined in the previous section. Thus, we have only to determine δ_M together with these counterterms such that the second condition Eq. (63) is satisfied.

$\partial_M \overline{\Gamma}^{(2)}_\alpha(\boldsymbol{k}, \Omega, M)$ evaluated at $M = 0$ is nothing but an amputated one-particle irreducible (1PI) part of a composite Green function at the massless point (Fig. 5) [54–56,61]. To see this, let us take the derivative of Eq. (28) with respect to the renormalized mass,

$$\partial_M \overline{\Gamma}^{(2)}_\alpha(\boldsymbol{k}, \Omega, M)\big|_{\boldsymbol{k}=0,M=0} = -\overline{G}^{-1}_\alpha \cdot \partial_M \overline{G}^{(2)}_\alpha(\boldsymbol{k}, \Omega, M)\big|_{\boldsymbol{k}=0,M=0} \cdot \overline{G}^{-1}_\alpha. \tag{66}$$

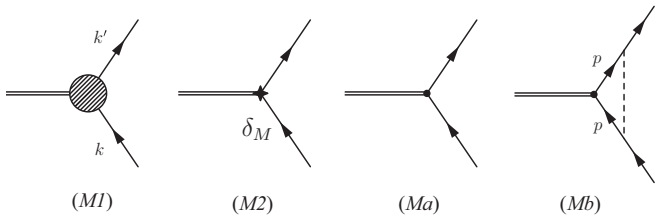

FIG. 5. (M1) Feynman diagrams of the 1-particle irreducible (1PI) part of $(1+\delta_M)\overline{\Gamma}^{(2,1)}_\alpha(\boldsymbol{k},\Omega)$. $(M2)$ The zeroth order in g for $\delta_M\overline{\Gamma}^{(2,1)}_\alpha(\boldsymbol{k},\Omega)$. (Ma) The zeroth order in g for $\overline{\Gamma}^{(2,1)}_\alpha(\boldsymbol{k},\Omega)$. (Mb) The first order in g for $\overline{\Gamma}^{(2,1)}_\alpha(\boldsymbol{k},\Omega)$.

From Eqs. (29) and (59), the derivative of the two-point Green function in the right-hand side is given by the following composite Green function,

$$\begin{aligned}
&(2\pi)^{d+1}\delta^{d+1}(k-k')\,\partial_M\overline{G}^{(2)}_\alpha(\boldsymbol{k},\Omega,M)\big|_{M=0}\\
&\quad=-(1+\delta_M)\int_{k''}\langle\phi_\alpha(k)\phi^\dagger_\epsilon(k'')\hat{\gamma}\phi_\epsilon(k'')\phi^\dagger_\alpha(k')\rangle_{\mathrm{eff},c},\\
&\quad\equiv-(1+\delta_M)(2\pi)^{d+1}\delta^{d+1}(k-k')\\
&\qquad\times\overline{G}_\alpha(\boldsymbol{k},\Omega)\overline{\Gamma}^{(2,1)}_\alpha(\boldsymbol{k},\Omega)\overline{G}_\alpha(\boldsymbol{k},\Omega),
\end{aligned}\tag{67}$$

with $\langle\cdots\rangle_{\mathrm{eff},c}\equiv\langle\phi_\alpha\phi^\dagger_\epsilon\hat{\gamma}\phi_\epsilon\phi^\dagger_\alpha\rangle_{\mathrm{eff}}-\langle\phi_\alpha\phi^\dagger_\alpha\rangle_{\mathrm{eff}}\langle\phi^\dagger_\epsilon\hat{\gamma}\phi_\epsilon\rangle_{\mathrm{eff}}$, $k\equiv(\boldsymbol{k},\omega)$, $k'\equiv(\boldsymbol{k}',\omega')$, and $k''\equiv(\boldsymbol{k}'',\omega'')$. Here $\langle\cdots\rangle_{\mathrm{eff}}$ in the right-hand side is taken over S_{eff} with the zero uniform mass, $M=0$. The two inverse Green functions in Eq. (66) amputate one-particle reducible parts of the composite Green function:

$$\partial_M\Gamma^{(2)}_\alpha(\boldsymbol{k},\Omega,M)\big|_{M=0}=(1+\delta_M)\overline{\Gamma}^{(2,1)}_\alpha(\boldsymbol{k},\Omega).\tag{68}$$

In the following, the 1PI part of the amputated composite Green function $\overline{\Gamma}^{(2,1)}_\alpha(\boldsymbol{k},\Omega)$ will be calculated at $\boldsymbol{k}=0$ perturbatively in g in $d=2-\epsilon$ with the renormalized massless theory S_{eff} of Eqs. (23) and (24). The 1PI part thus obtained contains $1/\epsilon$ divergent terms. δ_M in the right-hand side of Eq. (68) shall be chosen in such a way that all the $1/\epsilon$ divergent terms in $\overline{\Gamma}^{(2,1)}_\alpha(\boldsymbol{k}=0,\Omega)$ are canceled by δ_M, satisfying Eq. (63).

The zeroth and the first-order contributions to the right-hand side of Eq. (68) are shown in Fig. 5. $[Ma]$ and $[M2]$ comprise the zeroth order contribution to the 1PI part of $(1+\delta_M)\overline{\Gamma}^{(2,1)}_\alpha(\boldsymbol{k},\Omega)$:

$$[Ma]=\hat{\gamma},\quad [M2]=\delta^{(1)}_M\hat{\gamma}.$$

As in Eq. (44), $\delta^{(m)}_M$ stands for the m-loop contribution to the counterterm δ_M; $\delta_M\equiv\sum_m\delta^{(m)}_M$. A one-loop diagram $[Mb]$ is the first-order contribution to $\overline{\Gamma}^{(2,1)}_\alpha(\boldsymbol{k},\Omega)$:

$$\begin{aligned}
[Mb]&=\kappa\Omega^\epsilon\int_p\frac{1}{-i\Omega-\boldsymbol{\gamma}\cdot\boldsymbol{p}}\cdot\frac{1}{-i\Omega+\boldsymbol{\gamma}\cdot\boldsymbol{p}}\hat{\gamma}\\
&=\kappa\Omega^\epsilon\cdot\Big(-\frac{C_{2-\epsilon}}{\epsilon}\Omega^{-\epsilon}\Big)\hat{\gamma}+\mathcal{O}(1)=-\frac{g}{2\epsilon}\hat{\gamma}+\mathcal{O}(1).
\end{aligned}\tag{69}$$

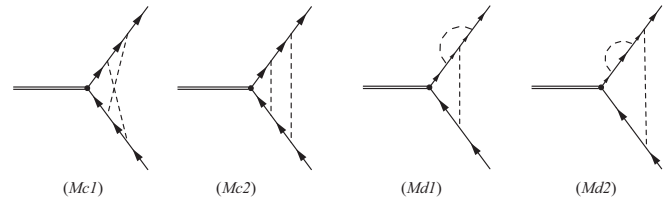

FIG. 6. Two-loop Feynman diagrams of the 1PI part of $(1+\delta_M)\overline{\Gamma}^{(2,1)}_\alpha(\boldsymbol{k},\Omega)$.

The one-loop counterterm $\delta^{(1)}_M$ should cancel this $1/\epsilon$ divergence,

$$\delta^{(1)}_M=\frac{g}{2\epsilon}.\tag{70}$$

The two-loop contributions to the 1PI part of $(1+\delta_M)\overline{\Gamma}^{(2,1)}_\alpha(\boldsymbol{k},\Omega)$ are shown in Figs. 6 and 7. All these diagrams are evaluated at $\boldsymbol{k}=0$, and take a form of $\hat{\gamma}$ (see below). We will evaluate their coefficients of $\hat{\gamma}$ in the following. The coefficient of $\hat{\gamma}$ in the diagram $[Mc1]$ is calculated as follows:

$$\begin{aligned}
[Mc1]&=\kappa^2\Omega^{2\epsilon}\int_{p,q}\frac{1}{-i\Omega+\boldsymbol{\gamma}\cdot\boldsymbol{q}}\cdot\frac{1}{-i\Omega-\boldsymbol{\gamma}\cdot\boldsymbol{p}}\\
&\qquad\times\frac{1}{-i\Omega+\boldsymbol{\gamma}\cdot\boldsymbol{p}}\cdot\frac{1}{-i\Omega-(\boldsymbol{\gamma}\cdot\boldsymbol{p}-\boldsymbol{\gamma}\cdot\boldsymbol{q})}\\
&=-\kappa^2\Omega^{2\epsilon}\int_{p,q}\frac{\boldsymbol{p}\boldsymbol{q}+q^2-\Omega^2}{(\Omega^2+\boldsymbol{q}^2)(\Omega^2+\boldsymbol{p}^2)(\Omega^2+(\boldsymbol{p}+\boldsymbol{q})^2)}\\
&=\kappa^2\Omega^{2\epsilon}\Big[\frac{1}{2}\Big(\frac{C_d}{\epsilon}\Omega^{-\epsilon}\Big)^2-\Big(\frac{C_d}{\epsilon}\Omega^{-\epsilon}\Big)^2\Big]+\mathcal{O}(1)\\
&=-\frac{1}{2}\frac{g^2}{4\epsilon^2}+\mathcal{O}(1).
\end{aligned}\tag{71}$$

The coefficients of $\hat{\gamma}$ in the diagrams $[Mc2]$, $[Md1]$, and $[Md2]$ are calculated as follows:

$$\begin{aligned}
[Mc2]&=\kappa^2\Omega^{2\epsilon}\int_{p,q}\frac{1}{-i\Omega+\boldsymbol{\gamma}\cdot\boldsymbol{q}}\cdot\frac{1}{-i\Omega-\boldsymbol{\gamma}\cdot\boldsymbol{p}}\\
&\qquad\times\frac{1}{-i\Omega+\boldsymbol{\gamma}\cdot\boldsymbol{p}}\cdot\frac{1}{-i\Omega-\boldsymbol{\gamma}\cdot\boldsymbol{q}}\\
&=\kappa^2\Omega^{2\epsilon}\Big(\frac{C_{2-\epsilon}}{\epsilon}\Omega^{-\epsilon}+\mathcal{O}(\epsilon)\Big)^2=\frac{g^2}{4\epsilon^2}+\mathcal{O}(1),
\end{aligned}\tag{72}$$

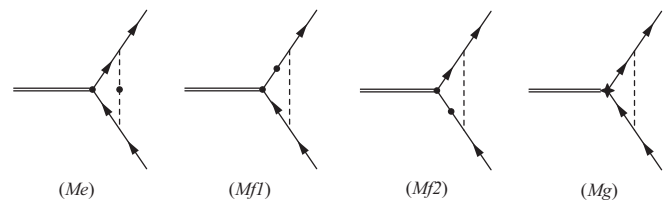

FIG. 7. Two-loop contributions to the 1PI part that contains one-loop counterterms, such as $\delta^{(1)}\kappa$, $\delta^{(1)}\Omega$, and $\delta^{(1)}_M$. Note that as shown in the previous section, δ_2 starts from the second order in g, so that it does not contribute to these diagrams.

$$[Md1] = \kappa^2\Omega^{2\epsilon}\int_{\boldsymbol{p},\boldsymbol{q}} \overline{G}_0(\boldsymbol{q})\overline{G}_0(-\boldsymbol{q}-\boldsymbol{p})\overline{G}_0(\boldsymbol{p})\overline{G}_0(-\boldsymbol{p})$$
$$= \kappa^2\Omega^{2\epsilon}\frac{1}{2}\Big(\frac{C_d}{\epsilon}\Omega^{-\epsilon}\Big)^2 + \mathcal{O}(1) = \frac{g^2}{8\epsilon^2} + \mathcal{O}(1), \quad (73)$$
$$[Md2] = \kappa^2\Omega^{2\epsilon}\int_{\boldsymbol{p},\boldsymbol{q}} \overline{G}_0(\boldsymbol{p})\overline{G}_0(-\boldsymbol{q})\overline{G}_0(\boldsymbol{p})\overline{G}_0(-\boldsymbol{p})$$
$$= \frac{g^2}{8\epsilon} + \mathcal{O}(1). \quad (74)$$

The two-loop contributions to $(1+\delta_M)\overline{\Gamma}^{(2,1)}_\alpha(\boldsymbol{k},\Omega)$ that contain one-loop counterterms are shown in Fig. 7. The diagram $[Me]$ contains $\delta\kappa$'s one-loop counterterm,

$$[Me] = \Omega^\epsilon\delta^{(1)}\kappa\int_{\boldsymbol{p}} \frac{1}{-i\Omega-\boldsymbol{\gamma}\cdot\boldsymbol{p}}\cdot\frac{1}{-i\Omega+\boldsymbol{\gamma}\cdot\boldsymbol{p}}$$
$$= \frac{\Omega^\epsilon}{2C_d}\frac{g^2}{\epsilon}\Big(-\frac{C_{2-\epsilon}}{\epsilon}\Omega^{-\epsilon} + \mathcal{O}(\epsilon)\Big) = -\frac{g^2}{2\epsilon^2} + \mathcal{O}(1). \quad (75)$$

The diagrams $[Mf1]$ and $[Mf2]$ are the κ's first-order terms that contain the $\delta\Omega$'s one-loop counterterm. A sum of these two is calculated as follows:

$$[Mf1] + [Mf2] = 2\kappa\Omega^\epsilon i\delta^{(1)}\Omega\int_{\boldsymbol{p}} \overline{G}_0(\boldsymbol{p})\overline{G}_0(\boldsymbol{p})\overline{G}_0(-\boldsymbol{p})$$
$$= 2\kappa\Omega^\epsilon(-i\Omega)^2\frac{g}{2\epsilon}\Big[\frac{1}{2}C_{2-\epsilon}\Omega^{-2-\epsilon} + \mathcal{O}(\epsilon)\Big]$$
$$= -\frac{g^2}{4\epsilon} + \mathcal{O}(1). \quad (76)$$

The diagram $[Mg]$ is the κ's first-order contribution to $\delta_M\overline{\Gamma}^{(2,1)}_\alpha(\boldsymbol{k},\Omega)$. Up to the second order in g, we use Eq. (70) as δ_M,

$$[Mg] = \delta_M^{(1)}\cdot\kappa\Omega^\epsilon\int_{\boldsymbol{p}} \frac{1}{-i\Omega-\boldsymbol{\gamma}\cdot\boldsymbol{p}}\cdot\frac{1}{-i\Omega+\boldsymbol{\gamma}\cdot\boldsymbol{p}}$$
$$= \frac{g}{2\epsilon}\cdot\kappa\Omega^\epsilon\int_{\boldsymbol{p}} \frac{-1}{\Omega^2+p^2} = -\frac{g^2}{4\epsilon^2} + \mathcal{O}(1). \quad (77)$$

By taking into account appropriate symmetry factors in each diagram, we let the two-loop counterterm $\delta_M^{(2)}$ cancels the $1/\epsilon$ divergent terms in Eq. (68):

$$\delta_M^{(2)} = -([Mc1] + [Mc2] + 2[Md1] + 2[Md2]$$
$$+ [Me] + [Mf1] + [Mf2] + [Mg]) = \frac{3g^2}{8\epsilon^2}. \quad (78)$$

Combining Eqs. (70) and (78), we finally obtain the mass renormalization constant $Z_{\mathcal{O}}$ up to the two-loop level as follows:

$$Z_{\mathcal{O}}^{-1} = Z_2^{-1}\big(1+\delta_M^{(1)}+\delta_M^{(2)}\big) = 1 + \frac{g}{2\epsilon} - \frac{g^2}{16\epsilon} + \frac{3g^2}{8\epsilon^2}. \quad (79)$$

The two-point vertex function has been renormalized up to the linear order in the uniform mass, Eq. (65). The UV divergent terms of the bare two-point vertex function are included in the renormalization constants at the finite RG scale Ω. The renormalized vertex functions in the small Ω limit determine ground-state property of S_{eff} with a finite uniform mass. When the RG scale Ω goes to zero with fixed bare uniform mass m and a fixed bare disorder strength Δ_3, the renormalized mass M changes its value according to Eq. (61). The renormalized M thus changed determines the ground-state property of S_{eff} with a finite (but small) uniform mass (see below). To determine how M changes in the small Ω limit, let us take an Ω derivative of Eq. (61) with a fixed m and Δ_3,

$$0 \equiv \frac{\partial\ln m}{\partial\ln\Omega}\Big|_{\Delta_3,m} = \frac{\partial\ln M}{\partial\ln\Omega}\Big|_{\Delta_3,m} - \frac{\partial\ln Z_{\mathcal{O}}}{\partial\ln\Omega}\Big|_{\Delta_3,m}. \quad (80)$$

This gives an anomalous dimension of the uniform mass, $\gamma_{\mathcal{O}}$,

$$\frac{\partial\ln M}{\partial\ln\Omega}\Big|_{\Delta_3,m} = \frac{\partial g}{\partial\ln\Omega}\Big|_{\Delta_3,m}\frac{d\ln Z_{\mathcal{O}}}{dg}$$
$$= \beta_g\frac{d\ln Z_{\mathcal{O}}}{dg} \equiv \gamma_{\mathcal{O}}. \quad (81)$$

From Eqs. (79) and (56), we obtain the two-loop evaluation of the anomalous dimension of the uniform mass:

$$\gamma_{\mathcal{O}} \equiv \beta_g\frac{\partial\ln Z_{\mathcal{O}}}{\partial g} = \frac{g}{2} - \frac{g^2}{8}. \quad (82)$$

In the clean limit ($g=0$), $\gamma_{\mathcal{O}}=0$, while $\gamma_{\mathcal{O}}$ can be nonzero around a fixed point with finite g. With an introduction of a renormalized dimensionless uniform mass ρ_m as $M \equiv \Omega\rho_m$, a scaling property of ρ_m around the massless theory is obtained as follows:

$$\frac{\partial\rho_m}{\partial l} = (1-\gamma_{\mathcal{O}})\rho_m \equiv d_m\rho_m, \quad (83)$$

with $l \equiv -\ln\Omega$. The two-loop scaling dimension of the renormalized dimensionless uniform mass is finally obtained around a massless fixed point ($\rho_m = 0$) as

$$d_m = 1 - \frac{g}{2} + \frac{g^2}{8}. \quad (84)$$

V. RG PHASE DIAGRAM OF TWO-DIMENSIONAL DIRAC FERMION WITH RANDOM MASS

In the previous section, the two-loop RG equations for the disorder strength and uniform mass as well as the dynamical exponent are evaluated perturbatively in the disorder strength around the clean-limit fixed point in $d = 2-\epsilon$, Eqs. (56), (84), and (57). In this section, we set $\epsilon = 0$, and study a structure of a RG phase diagram for the random-mass Dirac fermions in the two dimensions,

$$\frac{\partial g}{\partial l} = -\beta_g = -g^2 + \frac{g^3}{2},$$
$$\frac{\partial\rho_m}{\partial l} = d_m\rho_m = \Big(1 - \frac{g}{2} + \frac{g^2}{8}\Big)\rho_m, \quad (85)$$
$$z = 1 + \frac{g}{2} + \frac{g^2}{8}. \quad (86)$$

Here g, ρ_m, and z stand for the dimensionless random-mass-type disorder strength, the dimensionless uniform mass, and the dynamical exponent, respectively.

In the low-energy limit ($l \to +\infty$), the two coupling constants flow in the g-ρ_m parameter space, forming a phase diagram as shown in Fig. 1. The RG phase diagram comprises of three phases, a diffusive thermal metal (DTM) with larger g, a topological superconductor (TS) with $g=0$ and $\rho_m > 0$,

and a conventional Anderson insulator (AI) with $g = 0$ and $\rho_m < 0$. The three phases meet at an IR unstable fixed point at $(g, \rho_m) = (g_c, 0)$, that can be regarded as the multicritical (tricritical) point in the preceding numerical phase diagram of the CF model [11,14].

In the massless case ($\rho_m = 0$), the fixed point at $g = g_c$ corresponds to a semimetal-metal (SM-M) quantum phase transition point. For $g < g_c$ and $\rho_m = 0$, the finite disorder strength is renormalized to zero in the low-energy limit, where the ground state is characterized by the clean-limit massless Dirac-fermion fixed point at $(g, \rho_m) = (0, 0)$ (semimetal phase). For $g > g_c$, the disorder strength grows up into a larger value. The ground state for $g > g_c$ is in a diffusive metal phase, which is presumably described by another stable fixed point at larger g. The criticality of the SM-M quantum phase transition point at $\rho_m = 0$ is controlled by the fixed point at $g = g_c$. Since the weak disorder strength ($g < g_c$) is renormalized to zero, universality class of a phase transition between AI and TS phases is determined by the clean-limit massless Dirac-fermion fixed point. According to the mapping between the random-mass Dirac fermion model and the random-bond Ising model (RBIM), the massless Dirac-fermion fixed point corresponds to the clean-limit Ising fixed point in the RBIM [11].

The renormalized uniform mass is a relevant operator not only around the clean-limit massless Dirac-fermion fixed point but also around the fixed point at $g = g_c$. Accordingly, universality classes of the phase transition(s) between AI and DTM as well as that between TS and DTM must be determined by other saddle-point fixed point(s) at finite ρ_m. Exploring these fixed points at finite ρ_m goes beyond the scope of this paper and we leave it for future study. Two-loop evaluations of the critical disorder strength, the scaling dimensions of the disorder strength and the uniform mass, and the dynamical exponent around the unstable fixed point are $g_c = 2$, $\dim[g - g_c] = 2$, $\dim[\rho_m] = 1/2$, and $z(g_c) = 5/2$, respectively.

A correlation-length critical exponent for the SM-M quantum phase transition at the massless case is obtained from the following relation:

$$\frac{\partial \ln(g - g_c)}{\partial l} = \nu^{-1}, \tag{87}$$

with $\nu(g_c) = 1/2$ at the two-loop level. This critical exponent violates the Chayes inequality, that dictates $\nu d \geqslant 2$ with the spatial dimension d [62]. To see whether the inequality holds or not at the higher order in g, we evaluate in the next section the correlation-length critical exponent up to the four-loop level, using a relation between the effective theory S_{eff} and SU(N) Gross-Neveu (GN) model.

VI. HIGHER-LOOP RESULTS DEDUCED FROM MAPPINGS TO OTHER MODELS

A. Transformation between random-mass and random-chemical-potential in Dirac fermions in two dimensions

The two-loop RG equation [Eq. (85)] is consistent with the previous studies of random Dirac fermion with chemical-potential-type disorder, under a transformation between random mass and random chemical potential [33,34]. To explain this transformation, we start from the 2D replicated action for the random-mass Dirac fermion Eq. (9),

$$S_0 = \int d\tau d^2\boldsymbol{x}\, \psi_\alpha^\dagger \{\partial_\tau - iv(\partial_1\sigma_1 + \partial_2\sigma_2) + m\sigma_3\}\psi_\alpha,$$
$$S_1 = -\frac{\Delta_3}{2}\int d\tau d\tau' d^2\boldsymbol{x} (\psi_\alpha^\dagger\sigma_3\psi_\alpha)_{\boldsymbol{x},\tau}(\psi_\beta^\dagger\sigma_3\psi_\beta)_{\boldsymbol{x},\tau'}. \tag{88}$$

In the path integral formulation, $\psi^\dagger$ and ψ can be considered as independent integral variables. Thus, we can define a new set of integral variables $\{\bar\psi, \psi\}$ as [63]

$$\psi^\dagger \to \bar\psi = -i\psi^\dagger\sigma_3, \quad \psi^\dagger = i\bar\psi\sigma_3, \tag{89}$$

while keeping ψ unchanged. The action of Eq. (88) with $\{\bar\psi, \psi\}$ is given by

$$S_0 = \int d\tau d^2\boldsymbol{x}\, \bar\psi_\alpha \{(i\sigma_3)\partial_\tau + iv(\sigma_2\partial_1 - \sigma_1\partial_2) + im\}\psi_\alpha,$$
$$S_1 = +\frac{\Delta_3}{2}\int d\tau d\tau' d^2\boldsymbol{x}\, (\bar\psi_\alpha\psi_\alpha)_{\boldsymbol{x},\tau}(\bar\psi_\beta\psi_\beta)_{\boldsymbol{x},\tau'}. \tag{90}$$

Under an SU(2) rotation by the 90 degree,

$$\psi \to e^{i\frac{\pi}{4}\sigma_3}\psi, \quad \bar\psi \to \bar\psi e^{-i\frac{\pi}{4}\sigma_3},$$

the action with $\{\bar\psi, \psi\}$ can be put into the following form:

$$S_0 = \int d\tau d^2\boldsymbol{x}\, \bar\psi_\alpha \{(i\sigma_3)\partial_\tau - iv(\sigma_1\partial_1 + \sigma_2\partial_2) + im\}\psi_\alpha,$$
$$S_1 = +\frac{\Delta_3}{2}\int d\tau d\tau' d^2\boldsymbol{x}\, (\bar\psi_\alpha\psi_\alpha)_{\boldsymbol{x},\tau}(\bar\psi_\beta\psi_\beta)_{\boldsymbol{x},\tau'}. \tag{91}$$

This action is related to a replicated effective theory for the random Dirac fermion with the chemical-potential-type disorder potential [33,34,63],

$$S_0' = \int d\tau d^2\boldsymbol{x}\, \bar\psi_\alpha \{\partial_\tau - iv(\sigma_1\partial_1 + \sigma_2\partial_2) + \tilde m\sigma_3\}\psi_\alpha,$$
$$S_1' = -\frac{\Delta_0}{2}\int d\tau d\tau' d^2\boldsymbol{x}\, (\bar\psi_\alpha\psi_\alpha)_{\boldsymbol{x},\tau}(\bar\psi_\beta\psi_\beta)_{\boldsymbol{x},\tau'}. \tag{92}$$

Here $\tilde m$ and Δ_0 stand for bare uniform mass and chemical-potential-type disorder strength. The two theories are mapped to each other, where $i\partial_\tau$, im, and Δ_3 in Eq. (91) correspond to $\tilde m$ and ∂_τ and $-\Delta_0$ in Eq. (92), respectively. In the latter theory, the preceding work employed the renormalized single-particle energy as the RG scale and derive two-loop RG equation for the disorder strength Δ_0 [34,58,59,64]. One could also use the renormalized uniform mass as the RG scale, to derive the same two-loop RG equation. Thanks to the correspondence between Eqs. (91) and (92), such two-loop RG equation must be identical to Eq. (56) under the sign change of the disorder strength, $\Delta_0 \leftrightarrow -\Delta_3$. In fact, this is the case up to the two-loop level [34,58,59,64].

B. Relation to (1+1)-dimensional SU(N) Gross-Neveu model

The replicated 2D Dirac fermion theory with mass-type disorder Eq. (88) as well as that with chemical-potential-type disorder Eq. (92) are related to $(d+1)$D SU(N) Gross-Neveu (GN) model [64–66],

$$S_{\text{GN}} = \int d\tau d^d\boldsymbol{x}\left\{\bar\psi_a i(\partial_\mu\gamma^\mu - m)\psi_a + \frac{\bar g}{2}(\bar\psi_a\psi_a)^2\right\}, \tag{93}$$

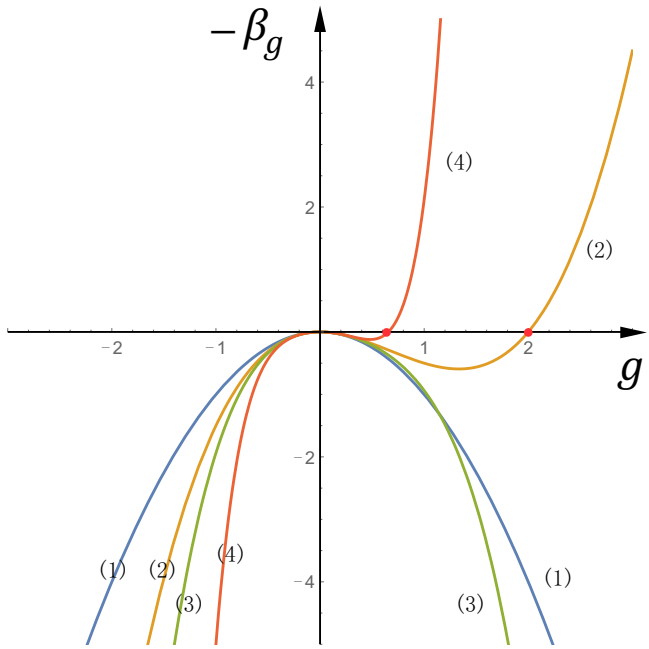

FIG. 8. The m-loop β function for coupling constant g with $m = 1, 2, 3, 4$. The two-loop and four-loop β function show a zero point at positive values of g.

with $a = 1, 2, \cdots, N$. The Dirac matrices $\{\gamma^\mu = \gamma_\mu\}$ $(\mu = 0, 1, \cdots, d)$ satisfy the relation $\{\gamma_\mu, \gamma_\nu\} = 2\delta_{\mu\nu}$ in $(d+1)$ Euclidean space time. The conjugate of the Dirac field is defined as $\bar{\psi} = i\psi^\dagger\gamma^0$. In the $(1+1)$-dimension, a representation of γ^μ matrices reduces to the two-by-two Pauli matrices,

$$\gamma^0 = \sigma_1, \quad \gamma^1 = \sigma_2, \quad \gamma^0\gamma^1 = i\sigma_3. \tag{94}$$

Note that the quenched disorder in Eq. (91) does not change the frequency of fermion lines, so that the fermion frequencies can be regarded as an external parameter. Accordingly, Eq. (91) in the two-spatial dimension in the zero replica limit $(R \to 0)$ and Eq. (93) in the $(1+1)$-dimension in the limit of $N \to 0$ share the same renormalization group theory, where ∂_1, ∂_2, Δ_3, m, and v in Eq. (91) are replaced by ∂_0, ∂_1, $\bar{g}$, m, and 1 in Eq. (93), respectively [66]. The β function for the GN coupling constant β_g and the anomalous dimension γ_m of the uniform mass m have been calculated up to the four-loop order [35,36]. In the limit of $N \to 0$, they are

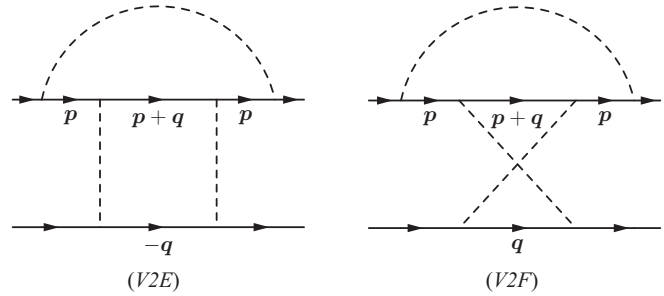

FIG. 10. Two-loop vertex diagrams.

given by

$$\beta_{\bar{g}}\big|_{N=0} = (d-2)\bar{g} + \frac{\bar{g}^2}{\pi} - \frac{\bar{g}^3}{2\pi^2} + \frac{7\bar{g}^4}{16\pi^3} - \frac{17\zeta_3 + 4}{8\pi^4}\bar{g}^5,$$
$$\gamma_m\big|_{N=0} = \frac{\bar{g}}{2\pi} - \frac{\bar{g}^2}{8\pi^2} + \frac{3\bar{g}^3}{32\pi^3} - \frac{[52\zeta_3 + 19]}{128\pi^4}\bar{g}^4, \tag{95}$$

where $\bar{g}$ corresponds to Δ_3 in Eq. (91). ζ_3 is a value of Riemann zeta function $\zeta_3 = \zeta(3)$ (Apéry's constant). To compare these equations with Eq. (85), we normalize $\bar{g} \equiv \Delta_3$ by π in the two dimensions from Eqs. (33) and (27):

$$g = 2C_2\Delta_3 = \frac{\bar{g}}{\pi}. \tag{96}$$

With this normalization, Eq. (95) is translated into the following β functions for g and the uniform mass ρ_m for the 2D random-mass Dirac fermions,

$$\frac{\partial g}{\partial l} = -g^2 + \frac{g^3}{2} - \frac{7}{16}g^4 + \frac{17\zeta_3 + 4}{8}g^5,$$
$$\frac{\partial \rho_m}{\partial l} = \left(1 - \frac{g}{2} + \frac{g^2}{8} - \frac{3g^3}{32} + \frac{52\zeta_3 + 19}{128}g^4\right)\rho_m. \tag{97}$$

At the two-loop level, Eq. (85) has the IR unstable fixed point at $g_c = 2$, which corresponds to the multicritical (tricritical) point. At the four-loop level, this critical disorder strength moves to a smaller value, $g_c \approx 0.655$. Figure 8 shows the β function of g for the one-, two-, three-, and four-loop order.

The four-loop evaluation of the scaling dimension of $g - g_c$ and the uniform mass around the fixed point are $\dim[g - g_c] \approx 1.66$ and $\dim[\rho_m] \approx 0.817$, respectively. The critical exponent associated with the SM-M quantum phase transition is evaluated as $\nu \approx 0.60$, which also violates the Chayes inequality.

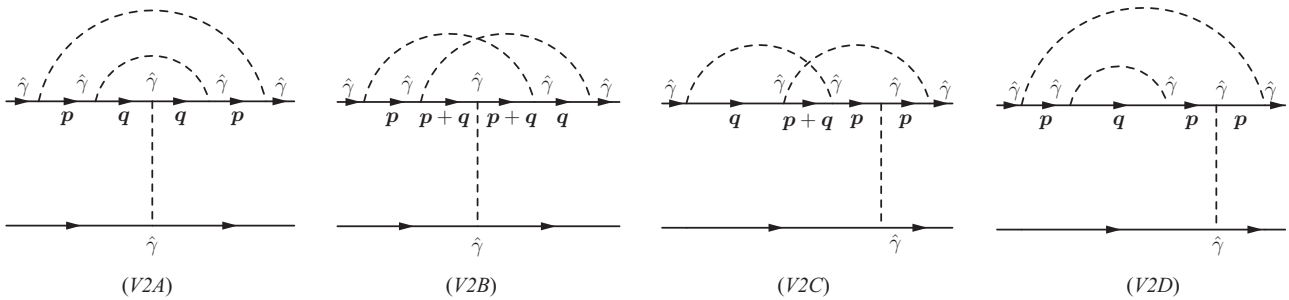

FIG. 9. Two-loop vertex diagrams.

VII. SUMMARY AND DISCUSSION

In summary, we have performed renormalization group analyses for the 2D Dirac fermion with the random-mass-type disorder. We obtained the two-loop β function for the disorder strength and observed an infrared unstable fixed point at a finite disorder strength. The fixed point corresponds to the quantum tricritical point that intervenes diffusive metal phase, and two topologically distinct gapped phases in two-dimensional class-D models. Two phase transition lines between the diffusive metal and the two gapped phases and a transition line between the two topologically distinct gapped phases meet at the tricritical point. The dynamical exponent and scaling dimension of the uniform mass are also evaluated at the tricritical point up to the two-loop level.

The two-loop evaluations of the scaling dimensions of the uniform mass and disorder strength shows that (i) the transition line between the two gapped phases is controlled by the clean-limit massless-Dirac-fermion fixed point with the Ising criticality, (ii) the transition lines between the diffusive metal phase and gapped phases are controlled *not* by the tricritical point *but* by another saddle-point fixed point with finite uniform Dirac mass. Using a mapping between the effective theory for the 2D random-mass Dirac fermion and (1+1)D SU(N) Gross-Neveu model in the limit of $N \to 0$, we also obtained the four-loop evaluations of the scaling dimensions of the uniform mass and disorder strength around the tricritical point. The four-loop result gives the same conclusion as the two-loop result about the criticality of the three transition lines. We found that the critical exponent ν for the semimetal-metal(SM-M) quantum phase transition breaks the Chayes inequality ($\nu d \geqslant 2$) both at the two-loop level and at the four-loop level, indicating an unusual aspect of the disorder-driven SM-M quantum phase transition in 2D class-D models.

ACKNOWLEDGMENTS

The authors thank Ilya Gruzberg for helpful discussions. Z.P., T.W., and R.S. were supported by the National Basic Research Programs of China (Grant No. 2019YFA0308401) and by National Natural Science Foundation of China (Grants No. 11674011 and No. 12074008). T.O. was supported by JSPS KAKENHI Grant No. 19H00658.

APPENDIX A: DISORDERED DIRAC HAMILTONIAN AND REPLICATED DIRAC-FERMIONS ACTION

In the main text, the renormalization of the Green functions of replicated Driac fermions is intensively studied. The study leads to the renormalization group equation for the 2D Dirac fermions with random mass. In this Appendix, we review an equivalence between averaged Green functions for disordered Dirac Hamiltonian and Green functions for the replicated Dirac fermions action $S_{\rm eff}$. A partition function for the disordered Dirac Hamiltonian is considered,

$$Z[\{V_3(\boldsymbol{r})\}] \equiv \int D\psi^\dagger D\psi\, e^{-S[\{V_3(\boldsymbol{r})\}]},\quad S[\{V_3(\boldsymbol{r})\}] \equiv \int_{-\beta/2}^{\beta/2} d\tau \left(\int d^2\boldsymbol{x}\psi^\dagger \partial_\tau \psi + \hat{H}[\{V_3(\boldsymbol{r})\}] \right), \tag{A1}$$

where an integral over an imaginary time τ ranges from $-\beta/2$ to $\beta/2$ with an inverse temperature $\beta \equiv 1/k_B T$. In the main text, we always take $\beta \to +\infty$ ($T = 0$). A time-ordered $2n$-point Green function is given by a trace over the action in Eq. (A1),

$$\langle \psi(1)\cdots\psi^\dagger(2n)\rangle = \frac{1}{Z}\int D\psi^\dagger D\psi\ \psi(1)\cdots\psi^\dagger(2n) e^{-S}, \tag{A2}$$

with space-time coordinates $i \equiv (\tau_i, \boldsymbol{x}_i)$ ($i = 1, \cdots, 2n$). The Green function is averaged over different disorder realization through the Gaussian distribution,

$$\langle(\cdots)\rangle_{\rm dis} \equiv \frac{1}{\mathcal{N}}\int DV_3\,(\cdots)\exp\Big[-\frac{1}{2\Delta_3}\int d^2\boldsymbol{x}V_3(\boldsymbol{x})^2\Big]. \tag{A3}$$

where $\mathcal{N}$ is a normalization factor such that $\langle 1\rangle_{\rm dis} = 1$. The averaged Green function is given by

$$\langle\langle\psi(1)\cdots\psi^\dagger(2n)\rangle\rangle_{\rm dis} = \frac{1}{\mathcal{N}}\int DV_3\,\langle\psi(1)\cdots\psi^\dagger(2n)\rangle\,\exp\left(-\frac{1}{2\Delta_3}\int V_3^2\right). \tag{A4}$$

To treat the disorder-averaged $2n$-point Green functions systematically, we use a replica method throughout the paper [53,54]. In the replica method, we introduce a replicated action that comprises of R-numbers of the identical free Dirac-fermion Hamiltonians of $\hat{H}_0$ and an elastic-scattering interaction between the replicated Dirac fermions, $S_{\rm eff}$ in Eq. (9). The averaged $2n$-point *connected* Green functions are given by the replica-limit of $2n$-point Green functions for the replicated Dirac-fermion action (9) [54]. The averaged two-point Green function is given by

$$\langle\langle\psi(\boldsymbol{x},\tau)\psi^\dagger(\boldsymbol{x}',\tau')\rangle\rangle_{\rm dis} = \lim_{R\to 0}\langle\psi_\alpha(\boldsymbol{x},\tau)\psi_\alpha^\dagger(\boldsymbol{x}',\tau')\rangle_{\rm eff}, \tag{A5}$$

where the summation over the replica index is *not* assumed in the right-hand side. $\langle\cdots\rangle_{\rm eff}$ in the right-hand side stands for a trace over the replicated action with the elastic interaction,

$$\langle\cdots\rangle_{\rm eff} \equiv \frac{1}{Z_{\rm eff}}\int D\psi_\alpha^\dagger D\psi_\alpha\,(\cdots)\,e^{-S_{\rm eff}},\ Z_{\rm eff} \equiv \int D\psi_\alpha^\dagger D\psi_\alpha\, e^{-S_{\rm eff}}. \tag{A6}$$

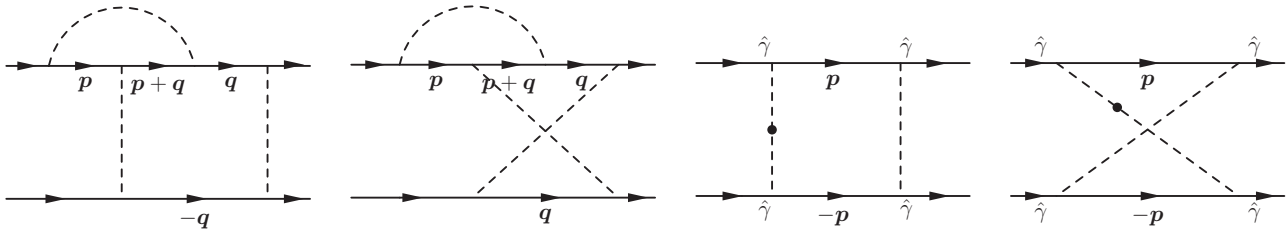

FIG. 11. Two-loop vertex diagrams.

The averaged four-point connected Green function is given by the four-point Green function of the replicated action in the replica limit,

$$\langle\langle\psi(1)\psi(2)\psi^\dagger(2')\psi^\dagger(1')\rangle_c\rangle_{\rm dis} = \lim_{R\to 0}\frac{1}{R}\sum_{\alpha_1,\alpha_2,\beta_2,\beta_1}\int D\psi^\dagger_\alpha D\psi_\alpha\,\psi_{\alpha_1}(1)\psi_{\alpha_2}(2)\psi^\dagger_{\beta_2}(2')\psi^\dagger_{\beta_1}(1')\,e^{-S_{\rm eff}},$$
$$= \lim_{R\to 0}\frac{1}{R}\sum_{\alpha_1,\alpha_2,\beta_2,\beta_1}\langle\psi_{\alpha_1}(1)\psi_{\alpha_2}(2)\psi^\dagger_{\beta_2}(2')\psi^\dagger_{\beta_1}(1')\rangle_{\rm eff}. \tag{A7}$$

Similarly, the equivalence between the disorder-averaged $2n$-point connected Green function of the disordered single-particle Hamiltonian and $2n$-point Green function of the replicated action in the replica limit holds true for the higher order.

APPENDIX B: TWO-LOOP RENORMALIZATION TO THE FOUR-POINT VERTEX FUNCTION

In this Appendix, the two-loop contribution to the four-point vertex counterterm is calculated in details. The two-loop contributions to the right-hand side of Eq. (32) are given by Feynman diagrams in Figs. 9–14. Note that each of them could have divergent terms with tensor forms other than $\hat\gamma\otimes\hat\gamma$. We will show in this Appendix that such divergent terms cancel exactly in the summation: the sum only gives divergent terms with the tensor form of $\hat\gamma\otimes\hat\gamma$. As in Eq. (32), the vertex function is evaluated with zero external momenta and with the two external frequencies set to Ω. Accordingly, all the internal fermion lines carry the same frequency Ω and we thus abbreviate $\overline{G}_0(\boldsymbol{p},\Omega)$ for internal fermion lines as $\overline{G}_0(\boldsymbol{p})$ in the following.

All the diagrams in Fig. 9 give the divergent terms with $\hat\gamma\otimes\hat\gamma$:

$$[V2A] = \kappa^3\Omega^{3\epsilon}\int_{\boldsymbol{p},\boldsymbol{q}}\hat\gamma\overline{G}_0(\boldsymbol{p})\hat\gamma\overline{G}_0(\boldsymbol{q})\hat\gamma\overline{G}_0(\boldsymbol{q})\hat\gamma\overline{G}_0(\boldsymbol{p})\hat\gamma\otimes\hat\gamma, \tag{B1}$$

$$[V2B] = \kappa^3\Omega^{3\epsilon}\int_{\boldsymbol{p},\boldsymbol{q}}\hat\gamma\overline{G}_0(\boldsymbol{p})\hat\gamma\overline{G}_0(\boldsymbol{p}+\boldsymbol{q})\hat\gamma\overline{G}_0(\boldsymbol{p}+\boldsymbol{q})\hat\gamma\overline{G}_0(\boldsymbol{q})\hat\gamma\otimes\hat\gamma, \tag{B2}$$

$$[V2C] = \kappa^3\Omega^{3\epsilon}\int_{\boldsymbol{p},\boldsymbol{q}}\hat\gamma\overline{G}_0(\boldsymbol{q})\hat\gamma\overline{G}_0(\boldsymbol{p}+\boldsymbol{q})\hat\gamma\overline{G}_0(\boldsymbol{p})\hat\gamma\overline{G}_0(\boldsymbol{p})\hat\gamma\otimes\hat\gamma, \tag{B3}$$

$$[V2D] = \kappa^3\Omega^{3\epsilon}\int_{\boldsymbol{p},\boldsymbol{q}}\hat\gamma\overline{G}_0(\boldsymbol{p})\hat\gamma\overline{G}_0(\boldsymbol{q})\hat\gamma\overline{G}_0(\boldsymbol{p})\hat\gamma\overline{G}_0(\boldsymbol{p})\hat\gamma\otimes\hat\gamma. \tag{B4}$$

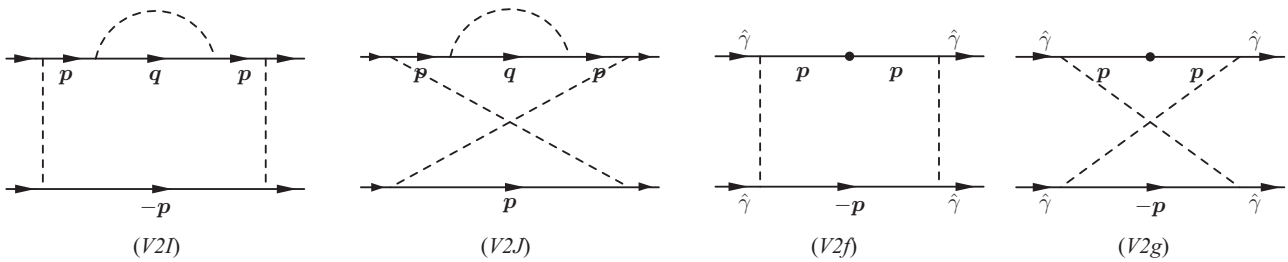

FIG. 12. Two-loop vertex diagrams.

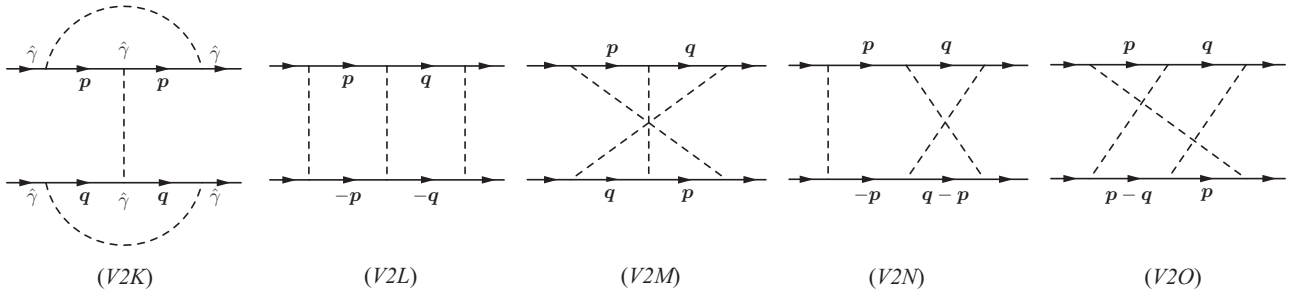

FIG. 13. Two-loop vertex diagrams.

These integrals always take the tensor-form of $\hat{\gamma}\otimes\hat{\gamma}$ and their coefficients are calculated as follows:

$$[V2A] = \kappa^3\Omega^{3\epsilon}\int_p \overline{G}_0(\boldsymbol{p})\frac{-1}{\Omega^2+q^2}\overline{G}_0(-\boldsymbol{p}) = \kappa^3\Omega^{3\epsilon}\Big(\int_p \frac{-1}{\Omega^2+p^2}\Big)^2$$
$$= \kappa^3\Omega^{3\epsilon}\Big(-\frac{C_{2-\epsilon}}{\epsilon}\Omega^{-\epsilon}\Big)^2 + \mathcal{O}(1) = \frac{\Omega^\epsilon}{2C_d}g\frac{g^2}{4\epsilon^2} + \mathcal{O}(1), \tag{B5}$$

$$[V2B] = \kappa^3\Omega^{3\epsilon}\int_{p,q}\frac{i\Omega-(\boldsymbol{\gamma}\cdot\boldsymbol{p})}{\Omega^2+p^2}\cdot\frac{-1}{\Omega^2+(\boldsymbol{p}+\boldsymbol{q})^2}\cdot\frac{i\Omega+(\boldsymbol{\gamma}\cdot\boldsymbol{q})}{\Omega^2+q^2} = \kappa^3\Omega^{3\epsilon}\int_{p,q}\frac{\Omega^2+(\boldsymbol{\gamma}\cdot\boldsymbol{q})(\boldsymbol{\gamma}\cdot\boldsymbol{p})}{(\Omega^2+p^2)[\Omega^2+(\boldsymbol{p}+\boldsymbol{q})^2](\Omega^2+q^2)}$$
$$= -\kappa^3\Omega^{3\epsilon}\frac{1}{2}\Big(\frac{C_{2-\epsilon}}{\epsilon}\Omega^{-\epsilon}\Big)^2 + \mathcal{O}(1) = -\frac{\Omega^\epsilon}{2C_d}g\frac{g^2}{8\epsilon^2} + \mathcal{O}(1), \tag{B6}$$

and

$$[V2C] = \kappa^3\Omega^{3\epsilon}\int_{p,q}\frac{i\Omega+(\boldsymbol{\gamma}\cdot\boldsymbol{q})}{\Omega^2+q^2}\cdot\frac{i\Omega-\boldsymbol{\gamma}(\boldsymbol{p}+\boldsymbol{q})}{\Omega^2+(\boldsymbol{p}+\boldsymbol{q})^2}\cdot\frac{-1}{\Omega^2+p^2}$$
$$= \kappa^3\Omega^{3\epsilon}\int_{p,q}\frac{1}{(\Omega^2+p^2)[\Omega^2+(\boldsymbol{p}+\boldsymbol{q})^2]} + \kappa^3\Omega^{3\epsilon}\int_{p,q}\frac{(\boldsymbol{\gamma}\cdot\boldsymbol{q})(\boldsymbol{\gamma}\cdot\boldsymbol{p})}{(\Omega^2+p^2)[\Omega^2+(\boldsymbol{p}+\boldsymbol{q})^2](\Omega^2+q^2)}$$
$$= \kappa^3\Omega^{3\epsilon}\Big(\frac{C_{2-\epsilon}}{\epsilon}\Omega^{-\epsilon}+\mathcal{O}(\epsilon)\Big)^2 - \kappa^3\Omega^{3\epsilon}\frac{1}{2}\Big(\frac{C_{2-\epsilon}}{\epsilon}\Omega^{-\epsilon}\Big)^2 + \mathcal{O}(1) = \frac{\Omega^\epsilon}{2C_d}g\frac{g^2}{8\epsilon^2} + \mathcal{O}(1), \tag{B7}$$

$$[V2D] = \kappa^3\Omega^{3\epsilon}\int_{p,q}\frac{i\Omega-(\boldsymbol{\gamma}\cdot\boldsymbol{p})}{\Omega^2+p^2}\cdot\frac{i\Omega+(\boldsymbol{\gamma}\cdot\boldsymbol{q})}{\Omega^2+q^2}\cdot\frac{-1}{\Omega^2+p^2} = \kappa^3\Omega^{3\epsilon}\int_{p,q}\frac{\Omega^2}{(\Omega^2+p^2)^2(\Omega^2+q^2)}$$
$$= \kappa^3\Omega^{3\epsilon}\Big(\frac{1}{2}C_{2-\epsilon}\Omega^{-\epsilon}+\mathcal{O}(\epsilon)\Big)\Big(\frac{C_{2-\epsilon}}{\epsilon}\Omega^{-\epsilon}+\mathcal{O}(\epsilon)\Big) = \frac{\Omega^\epsilon}{2C_d}g\frac{g^2}{8\epsilon} + \mathcal{O}(1). \tag{B8}$$

The second class of the two-loop contributions to the vertex function is shown in Figs. 10–12. These diagrams always take a form of $\gamma_0\otimes\gamma_0$; they do not contribute to the $\hat{\gamma}\otimes\hat{\gamma}$-type vertex. We will see that a sum of them is finite in the limit of $\epsilon\to 0$. A sum of diagram $[V2E]$ and diagram $[V2F]$ gives a finite order in small ϵ

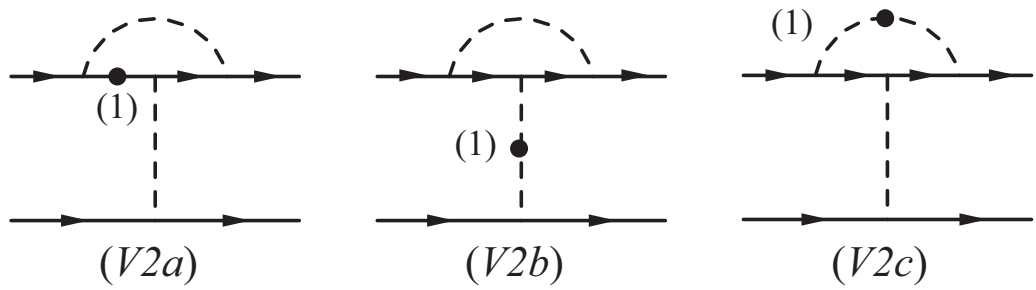

FIG. 14. Two-loop diagrams within one-loop counterterms.

limit,

$$[V2E]+[V2F]=\kappa^3\Omega^{3\epsilon}\int_{p,q}\overline{G}_0(-\boldsymbol{p})\overline{G}_0(\boldsymbol{p}+\boldsymbol{q})\overline{G}_0(-\boldsymbol{p})\otimes[\overline{G}_0(\boldsymbol{q})+\overline{G}_0(-\boldsymbol{q})]$$
$$=\kappa^3\Omega^{3\epsilon}\int_{p,q}\frac{i\Omega-(\boldsymbol{\gamma}\cdot\boldsymbol{p})}{\Omega^2+p^2}\cdot\frac{i\Omega+(\boldsymbol{\gamma}\cdot\boldsymbol{p}+\boldsymbol{\gamma}\cdot\boldsymbol{q})}{\Omega^2+(\boldsymbol{p}+\boldsymbol{q})^2}\cdot\frac{i\Omega-(\boldsymbol{\gamma}\cdot\boldsymbol{p})}{\Omega^2+p^2}\otimes\frac{2i\Omega}{\Omega^2+q^2}$$
$$=\kappa^3\Omega^{3\epsilon}\int_{p,q}\frac{2\Omega^4+2\Omega^2(p^2+2\boldsymbol{p}\boldsymbol{q})}{(\Omega^2+p^2)^2[\Omega^2+(\boldsymbol{p}+\boldsymbol{q})^2](\Omega^2+q^2)}\gamma_0\otimes\gamma_0=\mathcal{O}(1)\cdot\gamma_0\otimes\gamma_0. \tag{B9}$$

A sum of diagrams $[V2G]$ and $[V2H]$ has a $1/\epsilon$ singularity in the small ϵ limit,

$$[V2G]+[V2H]=\kappa^3\Omega^{3\epsilon}\int_{p,q}\overline{G}_0(-\boldsymbol{p})\overline{G}_0(\boldsymbol{p}+\boldsymbol{q})\overline{G}_0(-\boldsymbol{q})\otimes[\overline{G}_0(\boldsymbol{q})+\overline{G}_0(-\boldsymbol{q})]$$
$$=\kappa^3\Omega^{3\epsilon}\int_{p,q}\frac{i\Omega-(\boldsymbol{\gamma}\cdot\boldsymbol{p})}{\Omega^2+p^2}\cdot\frac{i\Omega+(\boldsymbol{\gamma}\cdot\boldsymbol{p}+\boldsymbol{\gamma}\cdot\boldsymbol{q})}{\Omega^2+(\boldsymbol{p}+\boldsymbol{q})^2}\cdot\frac{i\Omega-(\boldsymbol{\gamma}\cdot\boldsymbol{q})}{\Omega^2+q^2}\otimes\frac{2i\Omega}{\Omega^2+q^2}$$
$$=\kappa^3\Omega^{3\epsilon}\int_{p,q}\frac{2\Omega^4+2\Omega^2[p^2+q^2+(\boldsymbol{\gamma}\cdot\boldsymbol{p})(\boldsymbol{\gamma}\cdot\boldsymbol{q})]}{(\Omega^2+p^2)(\Omega^2+q^2)^2[\Omega^2+(\boldsymbol{p}+\boldsymbol{q})^2]}\gamma_0\otimes\gamma_0$$
$$=\kappa^3\Omega^{3\epsilon}\int_q\frac{2\Omega^2}{(\Omega^2+q^2)^2}\int_p\frac{1}{\Omega^2+p^2}\gamma_0\otimes\gamma_0+\mathcal{O}(1)=\kappa^3\Omega^{\epsilon}\frac{C_{2-\epsilon}}{\epsilon}C_{2-\epsilon}\gamma_0\otimes\gamma_0+\mathcal{O}(1). \tag{B10}$$

The singularity is canceled by the two-loop contributions $[V2d]$ and $[V2e]$ with the one-loop counterterm $\delta\kappa$:

$$[V2d]+[V2e]=\kappa\Omega^{\epsilon}\delta^{(1)}\kappa\cdot\Omega^{\epsilon}\int_p\overline{G}_0(-\boldsymbol{p})\otimes[\overline{G}_0(\boldsymbol{p})+\overline{G}_0(-\boldsymbol{p})]$$
$$=\kappa\Omega^{\epsilon}\cdot2\Omega^{\epsilon}\kappa^2\frac{C_{2-\epsilon}}{\epsilon}\cdot\int_p\frac{i\Omega-\boldsymbol{\gamma}\cdot\boldsymbol{p}}{\Omega^2+p^2}\otimes\frac{2i\Omega}{\Omega^2+p^2}=-2\kappa^3\Omega^{\epsilon}\frac{C_{2-\epsilon}}{\epsilon}C_{2-\epsilon}\gamma_0\otimes\gamma_0. \tag{B11}$$

Namely, with proper symmetry factors taken into account, the sum of these four diagrams gives a finite contribution in the small ϵ limit,

$$4[V2G]+4[V2H]+2[V2d]+2[V2e]=\mathcal{O}(1)\cdot\gamma_0\otimes\gamma_0. \tag{B12}$$

Diagrams $[V2I]$ and $[V2J]$ cancel each other,

$$[V2I]+[V2J]=\kappa^3\Omega^{3\epsilon}\int_{p,q}\overline{G}_0(-\boldsymbol{p})\overline{G}_0(\boldsymbol{q})\overline{G}_0(-\boldsymbol{p})\otimes[\overline{G}_0(\boldsymbol{p})+\overline{G}_0(-\boldsymbol{p})]$$
$$=\kappa^3\Omega^{3\epsilon}\int_{p,q}\frac{i\Omega-(\boldsymbol{\gamma}\cdot\boldsymbol{p})}{\Omega^2+p^2}\cdot\frac{i\Omega+(\boldsymbol{\gamma}\cdot\boldsymbol{q})}{\Omega^2+q^2}\cdot\frac{i\Omega-(\boldsymbol{\gamma}\cdot\boldsymbol{p})}{\Omega^2+p^2}\otimes\frac{2i\Omega}{\Omega^2+p^2}$$
$$=\kappa^3\Omega^{3\epsilon}\int_{p,q}\frac{\Omega^2-p^2}{(\Omega^2+p^2)^2(\Omega^2+q^2)}\otimes\frac{2\Omega^2}{\Omega^2+p^2}$$
$$=\kappa^3\Omega^{3\epsilon}2\Omega^2\int_p\frac{\Omega^2-p^2}{(\Omega^2+p^2)^3}\int_q\frac{1}{\Omega^2+q^2}\gamma_0\otimes\gamma_0. \tag{B13}$$

Here the momentum integral over $\boldsymbol{p}$ in the right-hand side reduces to zero,

$$\int_p\frac{2\Omega^2}{(\Omega^2+p^2)^3}-\int_p\frac{1}{(\Omega^2+p^2)^2}=2\Omega^2\frac{1}{4}C_{2-\epsilon}\Omega^{-4-\epsilon}-\frac{1}{2}C_{2-\epsilon}\Omega^{-2-\epsilon}=0.$$

Similarly, diagrams $(V2f)$ and $(V2g)$ cancel each other exactly:

$$[V2f]+[V2g]=i\delta^{(1)}\Omega\int_p\hat{\gamma}\overline{G}_0(\boldsymbol{p})\overline{G}_0(\boldsymbol{p})\hat{\gamma}\otimes[\overline{G}_0(\boldsymbol{p})+\overline{G}_0(-\boldsymbol{p})]$$
$$=i\delta^{(1)}\Omega\int_p\frac{-\Omega^2+p^2}{(\Omega^2+p^2)^2}\otimes\frac{2i\Omega}{\Omega^2+p^2}=-2\delta^{(1)}\Omega\,\Omega\int_p\frac{-\Omega^2+p^2}{(\Omega^2+p^2)^3}\gamma_0\otimes\gamma_0=0. \tag{B14}$$

We conclude that a sum of all the diagrams in Figs. 10–12 generate a $\gamma_0\otimes\gamma_0$-type term, while it has no divergence in the limit of $\epsilon\to0$. The third class of the two-loop diagrams for the vertex function is shown in Fig. 13. They give divergent terms with

the $\hat{\gamma}\otimes\hat{\gamma}$ tensor form. Diagram $[V2K]$ is calculated as follows:

$$[V2K] = \kappa^3\Omega^{3\epsilon}\int_{p,q}\hat{\gamma}\overline{G}_0(\boldsymbol{p})\hat{\gamma}\overline{G}_0(\boldsymbol{p})\hat{\gamma}\otimes\hat{\gamma}\overline{G}_0(\boldsymbol{p})\hat{\gamma}\overline{G}_0(\boldsymbol{p})\hat{\gamma} = \kappa^3\Omega^{3\epsilon}\int_{p,q}\frac{-1}{\Omega^2+p^2}\cdot\frac{-1}{\Omega^2+q^2}\hat{\gamma}\otimes\hat{\gamma}$$
$$= \kappa^3\Omega^{3\epsilon}\Big[\frac{C_{2-\epsilon}}{\epsilon}\Omega^{-\epsilon}+\mathcal{O}(\epsilon)\Big]^2\hat{\gamma}\otimes\hat{\gamma} = \Big(\kappa\Omega^{\epsilon}\frac{g^2}{4\epsilon^2}+\mathcal{O}(1)\Big)\hat{\gamma}\otimes\hat{\gamma} = \Big(\frac{\Omega^{\epsilon}}{2C_d}g\frac{g^2}{4\epsilon^2}+\mathcal{O}(1)\Big)\hat{\gamma}\otimes\hat{\gamma}. \tag{B15}$$

It is convenient to calculate a sum of $[V2L]$ and $[V2M]$:

$$[V2L]+[V2M] = \kappa^3\Omega^{3\epsilon}\int_{p,q}\overline{G}_0(-\boldsymbol{p})\overline{G}_0(\boldsymbol{q})\hat{\gamma}\otimes[\overline{G}_0(\boldsymbol{p})\overline{G}_0(-\boldsymbol{q})+\overline{G}_0(-\boldsymbol{q})\overline{G}_0(\boldsymbol{p})]\hat{\gamma}$$
$$= \kappa^3\Omega^{3\epsilon}\int_{p,q}\frac{i\Omega-(\boldsymbol{\gamma}\cdot\boldsymbol{p})}{\Omega^2+p^2}\cdot\frac{i\Omega+(\boldsymbol{\gamma}\cdot\boldsymbol{q})}{\Omega^2+q^2}\hat{\gamma}\otimes\Big[\frac{i\Omega+(\boldsymbol{\gamma}\cdot\boldsymbol{p})}{\Omega^2+p^2}\cdot\frac{i\Omega-(\boldsymbol{\gamma}\cdot\boldsymbol{q})}{\Omega^2+q^2}+\frac{i\Omega-(\boldsymbol{\gamma}\cdot\boldsymbol{q})}{\Omega^2+q^2}\cdot\frac{i\Omega+(\boldsymbol{\gamma}\cdot\boldsymbol{p})}{\Omega^2+p^2}\Big]\hat{\gamma}.$$

In the right-hand side, odd terms in $\boldsymbol{p}$ or $\boldsymbol{q}$ vanish:

$$[V2L]+[V2M] = 2\kappa^3\Omega^{3\epsilon}\int_{p,q}\frac{-\Omega^2-(\boldsymbol{\gamma}\cdot\boldsymbol{p})(\boldsymbol{\gamma}\cdot\boldsymbol{q})}{(\Omega^2+p^2)(\Omega^2+q^2)}\hat{\gamma}\otimes\frac{-\Omega^2-\boldsymbol{pq}}{(\Omega^2+p^2)(\Omega^2+q^2)}\hat{\gamma} \tag{B16}$$
$$+2\kappa^3\Omega^{3\epsilon}\int_{p,q}\frac{-i\Omega(\boldsymbol{\gamma}\cdot\boldsymbol{p}-\boldsymbol{\gamma}\cdot\boldsymbol{q})}{(\Omega^2+p^2)(\Omega^2+q^2)}\hat{\gamma}\otimes\frac{i\Omega(\boldsymbol{\gamma}\cdot\boldsymbol{p}-\boldsymbol{\gamma}\cdot\boldsymbol{q})}{(\Omega^2+p^2)(\Omega^2+q^2)}\hat{\gamma}. \tag{B17}$$

Under an exchange between $\boldsymbol{p}$ and $\boldsymbol{q}$ in the integrand, Eq. (B16) reduces to

$$(B16) = 2\kappa^3\Omega^{3\epsilon}\int_{p,q}\frac{(\Omega^2+\boldsymbol{pq})^2}{(\Omega^2+p^2)^2(\Omega^2+q^2)^2}\hat{\gamma}\otimes\hat{\gamma} = 2\kappa^3\Omega^{3\epsilon}\sum_{i,j}\int_{p,q}\frac{p_iq_ip_jq_j}{(\Omega^2+p^2)^2(\Omega^2+q^2)^2}\hat{\gamma}\otimes\hat{\gamma}+\mathcal{O}(1).$$

Those summands with $i\neq j$ vanish under the integral over $\boldsymbol{p}$ or $\boldsymbol{q}$. Those summands with $i=j$ give out

$$(B16) = 2\kappa^3\Omega^{3\epsilon}\sum_i\int_{p,q}\frac{p_i^2}{(\Omega^2+p^2)^2}\frac{q_i^2}{(\Omega^2+q^2)^2}\hat{\gamma}\otimes\hat{\gamma} = 2\kappa^3\Omega^{3\epsilon}\sum_i\int_p\frac{p_i^2}{(\Omega^2+p^2)^2}\frac{1}{d}\int_q\frac{q^2}{(\Omega^2+q^2)^2}\hat{\gamma}\otimes\hat{\gamma}$$
$$= \kappa^3\Omega^{3\epsilon}\frac{2}{d}\int_p\frac{p^2}{\big(\Omega^2+p^2\big)^2}\int_q\frac{q^2}{(\Omega^2+q^2)^2}\hat{\gamma}\otimes\hat{\gamma}.$$

The integral in the right-hand side is calculated as follows:

$$\int_p\frac{p^2}{(\Omega^2+p^2)^2} = \int_p\frac{1}{\Omega^2+p^2}-\int_p\frac{\Omega^2}{(\Omega^2+p^2)^2} = \frac{C_{2-\epsilon}}{\epsilon}\Omega^{-\epsilon}\Big(1-\frac{\epsilon}{2}\Big)+\mathcal{O}(\epsilon).$$

Thus, we finally have Eq. (B16) as

$$(B16) = \kappa^3\Omega^{3\epsilon}\frac{2}{d}\Big[\frac{C_{2-\epsilon}}{\epsilon}\Omega^{-\epsilon}\Big(1-\frac{\epsilon}{2}\Big)+\mathcal{O}(\epsilon)\Big]^2\hat{\gamma}\otimes\hat{\gamma}$$
$$= \Big[\kappa^3\Omega^{\epsilon}\frac{C_{2-\epsilon}^2}{\epsilon^2}-\kappa^3\Omega^{\epsilon}\frac{C_{2-\epsilon}^2}{2\epsilon}+\mathcal{O}(1)\Big]\hat{\gamma}\otimes\hat{\gamma} = \Big[\frac{\Omega^{\epsilon}}{2C_d}\frac{g^3}{4\epsilon^2}-\frac{\Omega^{\epsilon}}{2C_d}\frac{g^3}{8\epsilon}+\mathcal{O}(1)\Big]\hat{\gamma}\otimes\hat{\gamma}.$$

For Eq. (B17), those terms proportional to p_iq_j ($i=j$ or $i\neq j$) or to p_ip_j ($i\neq j$) vanish under the integral over $\boldsymbol{p}$ or $\boldsymbol{q}$,

$$(B17) = 2\kappa^3\Omega^{3\epsilon}\int_{p,q}\frac{-i\Omega(\boldsymbol{\gamma}\cdot\boldsymbol{p}-\boldsymbol{\gamma}\cdot\boldsymbol{q})}{(\Omega^2+p^2)(\Omega^2+q^2)}\hat{\gamma}\otimes\frac{i\Omega(\boldsymbol{\gamma}\cdot\boldsymbol{p}-\boldsymbol{\gamma}\cdot\boldsymbol{q})}{(\Omega^2+p^2)(\Omega^2+q^2)}\hat{\gamma} = 2\kappa^3\Omega^{3\epsilon}\int_{p,q}\frac{\Omega^2(\boldsymbol{p\gamma}\hat{\gamma}\otimes\boldsymbol{p\gamma}\hat{\gamma}+\boldsymbol{q\gamma}\hat{\gamma}\otimes\boldsymbol{q\gamma}\hat{\gamma})}{(\Omega^2+p^2)^2(\Omega^2+q^2)^2},$$
$$= 2\kappa^3\Omega^{3\epsilon}\sum_i\int_{p,q}\frac{\Omega^2\big(p_i^2+q_i^2\big)}{(\Omega^2+p^2)^2(\Omega^2+q^2)^2}\gamma_i\hat{\gamma}\otimes\gamma_i\hat{\gamma} = 2\kappa^3\Omega^{3\epsilon}\sum_i\frac{1}{d}\int_{p,q}\frac{\Omega^2(p^2+q^2)}{(\Omega^2+p^2)^2(\Omega^2+q^2)^2}\gamma_i\hat{\gamma}\otimes\gamma_i\hat{\gamma}$$
$$= \kappa^3\Omega^{3\epsilon}\sum_i\frac{1}{d}\int_p\frac{1}{\Omega^2+p^2}\int_q\frac{4\Omega^2}{(\Omega^2+q^2)^2}\gamma_i\hat{\gamma}\otimes\gamma_i\hat{\gamma}+\mathcal{O}(1)$$
$$= 2\kappa^3\Omega^{\epsilon}\frac{1}{d}\frac{C_{2-\epsilon}}{\epsilon}C_{2-\epsilon}\sum_i\gamma_i\hat{\gamma}\otimes\gamma_i\hat{\gamma}+\mathcal{O}(1).$$

Thus, the sum of $[V2L]$ and $[V2M]$ generates a divergent term with a tensor-form of $\gamma_i\hat{\gamma}\otimes\gamma_i\hat{\gamma}$. However, such divergent term is canceled by a sum of $[V2N]$ and $[V2O]$. The sum of $[V2N]$ and $[V2O]$ is calculated as

follows:

$$[V2N]+[V2O]=\kappa^3\Omega^{3\epsilon}\int_{p,q}\overline{G}_0(-\boldsymbol{p})\overline{G}_0(\boldsymbol{q})\hat{\gamma}\otimes[\overline{G}_0(\boldsymbol{p})\overline{G}_0(\boldsymbol{q}-\boldsymbol{p})+\overline{G}_0(\boldsymbol{q}-\boldsymbol{p})\overline{G}_0(\boldsymbol{p})]\hat{\gamma}$$
$$=\int_{p,q}\frac{i\Omega-(\boldsymbol{\gamma}\cdot\boldsymbol{p})}{\Omega^2+p^2}\cdot\frac{i\Omega+(\boldsymbol{\gamma}\cdot\boldsymbol{q})}{\Omega^2+q^2}\hat{\gamma}$$
$$\otimes\left[\frac{i\Omega+(\boldsymbol{\gamma}\cdot\boldsymbol{p})}{\Omega^2+p^2}\cdot\frac{i\Omega+(\boldsymbol{\gamma}\cdot\boldsymbol{q}-\boldsymbol{\gamma}\cdot\boldsymbol{p})}{\Omega^2+(\boldsymbol{q}-\boldsymbol{p})^2}+\frac{i\Omega+(\boldsymbol{\gamma}\cdot\boldsymbol{q}-\boldsymbol{\gamma}\cdot\boldsymbol{p})}{\Omega^2+(\boldsymbol{q}-\boldsymbol{p})^2}\cdot\frac{i\Omega+(\boldsymbol{\gamma}\cdot\boldsymbol{p})}{\Omega^2+p^2}\right]\hat{\gamma}.$$

In the right-hand side, odd terms in $\boldsymbol{p}$ or $\boldsymbol{q}$ vanish under the momentum integrals:

$$[V2N]+[V2O]=2\kappa^3\Omega^{3\epsilon}\int_{p,q}\frac{-\Omega^2-(\boldsymbol{\gamma}\cdot\boldsymbol{p})(\boldsymbol{\gamma}\cdot\boldsymbol{q})}{(\Omega^2+p^2)(\Omega^2+q^2)}\hat{\gamma}\otimes\frac{-\Omega^2+\boldsymbol{p}(\boldsymbol{q}-\boldsymbol{p})}{(\Omega^2+p^2)[\Omega^2+(\boldsymbol{q}-\boldsymbol{p})^2]}\hat{\gamma} \tag{B18}$$
$$+2\kappa^3\Omega^{3\epsilon}\int_{p,q}\frac{-i\Omega(\boldsymbol{\gamma}\cdot\boldsymbol{p}-\boldsymbol{\gamma}\cdot\boldsymbol{q})}{(\Omega^2+p^2)(\Omega^2+q^2)}\hat{\gamma}\otimes\frac{i\Omega(\boldsymbol{\gamma}\cdot\boldsymbol{q})}{(\Omega^2+p^2)[\Omega^2+(\boldsymbol{q}-\boldsymbol{p})^2]}\hat{\gamma}. \tag{B19}$$

Eq. (B18) takes the tensor form of $\hat{\gamma}\otimes\hat{\gamma}$, whose coefficient is calculated as follows:

$$(B18)=2\kappa^3\Omega^{3\epsilon}\int_{p,q}\frac{\Omega^2+(\boldsymbol{\gamma}\cdot\boldsymbol{p})(\boldsymbol{\gamma}\cdot\boldsymbol{q})}{(\Omega^2+p^2)(\Omega^2+q^2)}\cdot\frac{\Omega^2-\boldsymbol{p}(\boldsymbol{q}-\boldsymbol{p})}{(\Omega^2+p^2)[\Omega^2+(\boldsymbol{q}-\boldsymbol{p})^2]}\hat{\gamma}\otimes\hat{\gamma}$$
$$=\kappa^3\Omega^{3\epsilon}\int_{p,q}\frac{\Omega^2-(\boldsymbol{\gamma}\cdot\boldsymbol{p})(\boldsymbol{\gamma}\cdot\boldsymbol{q})}{(\Omega^2+p^2)}\cdot\frac{2\Omega^2+p^2-q^2+(\boldsymbol{q}+\boldsymbol{p})^2}{(\Omega^2+p^2)(\Omega^2+q^2)[\Omega^2+(\boldsymbol{q}+\boldsymbol{p})^2]}\hat{\gamma}\otimes\hat{\gamma}$$
$$=\kappa^3\Omega^{3\epsilon}\int_{p,q}\left\{\frac{-(\boldsymbol{\gamma}\cdot\boldsymbol{p})(\boldsymbol{\gamma}\cdot\boldsymbol{q})}{(\Omega^2+p^2)(\Omega^2+q^2)[\Omega^2+(\boldsymbol{q}+\boldsymbol{p})^2]}+\frac{\Omega^2}{(\Omega^2+p^2)^2(\Omega^2+q^2)}-\frac{1}{(\Omega^2+p^2)(\Omega^2+q^2)}\right\}\hat{\gamma}\otimes\hat{\gamma}+\mathcal{O}(1).$$

After the momentum integrals, each of the three integrands in the right-hand side are diverging with respect to small ϵ,

$$(B18)=\kappa^3\Omega^{3\epsilon}\left\{\frac{1}{2}\left(\frac{C_{2-\epsilon}}{\epsilon}\Omega^{-\epsilon}\right)^2+\left[\frac{C_{2-\epsilon}\Omega^{-\epsilon}}{2}+\mathcal{O}(\epsilon)\right]\left[\frac{C_{2-\epsilon}}{\epsilon}\Omega^{-\epsilon}+\mathcal{O}(\epsilon)\right]-\left[\frac{C_{2-\epsilon}}{\epsilon}\Omega^{-\epsilon}+\mathcal{O}(\epsilon)\right]^2+\mathcal{O}(1)\right\}\hat{\gamma}\otimes\hat{\gamma}$$
$$=\kappa^3\Omega^{\epsilon}\left\{\frac{1}{2}\frac{C_{2-\epsilon}^2}{\epsilon}-\frac{1}{2}\frac{C_{2-\epsilon}^2}{\epsilon^2}+\mathcal{O}(1)\right\}\hat{\gamma}\otimes\hat{\gamma}=\frac{\Omega^{\epsilon}}{2C_d}\left\{\frac{g^3}{8\epsilon}-\frac{g^3}{8\epsilon^2}+\mathcal{O}(1)\right\}\hat{\gamma}\otimes\hat{\gamma}.$$

Eq. (B19) takes the tensor form of $\gamma_i\hat{\gamma}\otimes\gamma_i\hat{\gamma}$, whose coefficient is calculated as follows,

$$(B19)=2\kappa^3\Omega^{3\epsilon}\int_{p,q}\frac{-i\Omega(\boldsymbol{\gamma}\cdot\boldsymbol{p}-\boldsymbol{\gamma}\cdot\boldsymbol{q})}{(\Omega^2+p^2)(\Omega^2+q^2)}\hat{\gamma}\otimes\frac{i\Omega(\boldsymbol{\gamma}\cdot\boldsymbol{q})}{(\Omega^2+p^2)[\Omega^2+(\boldsymbol{q}-\boldsymbol{p})^2]}\hat{\gamma}$$
$$=2\kappa^3\Omega^{3\epsilon}\Omega^2\frac{1}{d}\int_{p,q}\frac{\boldsymbol{q}\cdot\boldsymbol{p}-q^2}{(\Omega^2+p^2)^2(\Omega^2+q^2)[\Omega^2+(\boldsymbol{q}-\boldsymbol{p})^2]}\sum_i\gamma_i\hat{\gamma}\otimes\gamma_i\hat{\gamma}$$
$$=2\kappa^3\Omega^{3\epsilon}\Omega^2\frac{1}{d}\int_{p,q}\frac{-\boldsymbol{q}^2}{(\Omega^2+p^2)^2(\Omega^2+q^2)[\Omega^2+(\boldsymbol{q}-\boldsymbol{p})^2]}\sum_i\gamma_i\hat{\gamma}\otimes\gamma_i\hat{\gamma}+\mathcal{O}(1).$$

The first term in the right-hand side diverges in the small ϵ limit, taking the similar form as Eq. (B17) with the opposite sign:

$$(B19)=2\kappa^3\Omega^{3\epsilon}\Omega^2\frac{1}{d}\int_{p,q}\frac{-1}{(\Omega^2+p^2)^2(\Omega^2+(\boldsymbol{q}-\boldsymbol{p})^2)}\sum_i\gamma_i\hat{\gamma}\otimes\gamma_i\hat{\gamma}+\mathcal{O}(1)$$
$$=-\kappa^3\Omega^{3\epsilon}\frac{1}{d}\int_p\frac{2\Omega^2}{(\Omega^2+p^2)^2}\int_q\frac{1}{\Omega^2+\boldsymbol{q}^2}\sum_i\gamma_i\hat{\gamma}\otimes\gamma_i\hat{\gamma}+\mathcal{O}(1)$$
$$=-\kappa^3\Omega^{\epsilon}\frac{1}{d}\frac{C_{2-\epsilon}}{\epsilon}C_{2-\epsilon}\sum_i\gamma_i\hat{\gamma}\otimes\gamma_i\hat{\gamma}+\mathcal{O}(1).$$

Accordingly, the divergent terms in Eqs. (B17) and (B19) cancel each other in the sum of all the diagrams in Fig. 13 with proper symmetry factors. As a result, the sum of all the diagrams gives out only the divergent term with the tensor-form of $\hat{\gamma}\otimes\hat{\gamma}$:

$$[V2L]+[V2M]+2\big([V2N]+[V2O]\big)=(B16)+(B17)+2(B18)+2(B19)=\frac{\Omega^{\epsilon}}{2C_d}\frac{g^3}{8\epsilon}\hat{\gamma}\otimes\hat{\gamma}. \tag{B20}$$

The last class of the two-loop contributions to the vertex function is shown in Fig. 14. They take the tensor-form of $\hat{\gamma}\otimes\hat{\gamma}$. Their respective coefficients are calculated as follows:

$$[V2a] = \kappa^2\Omega^{2\epsilon}\, i\delta^{(1)}\Omega \int_p \overline{G}_0(-\boldsymbol{p})\overline{G}_0(+\boldsymbol{p})\overline{G}_0(+\boldsymbol{p})\hat{\gamma}\otimes\hat{\gamma} = \kappa^2\Omega^{2\epsilon} i\Omega\frac{g}{2\epsilon}\int_p \frac{i\Omega}{(\Omega^2+p^2)^2}\hat{\gamma}\otimes\hat{\gamma}$$

$$= \kappa^2\Omega^{2\epsilon}\big(i\Omega\big)^2\frac{g}{2\epsilon}\Big[\frac{1}{2}C_{2-\epsilon}\Omega^{-2-\epsilon}+\mathcal{O}(\epsilon)\Big]\hat{\gamma}\otimes\hat{\gamma} = -\frac{\Omega^\epsilon}{2C_d}g\frac{g^2}{8\epsilon}\hat{\gamma}\otimes\hat{\gamma}+\mathcal{O}(1), \tag{B21}$$

$$[V2b] = [V2c] = \kappa\Omega^\epsilon\,\Omega^\epsilon\delta^{(1)}\kappa\int_p \overline{G}_0(+\boldsymbol{p})\overline{G}_0(-\boldsymbol{p})\hat{\gamma}\otimes\hat{\gamma} = -\kappa\Omega^\epsilon\frac{\Omega^\epsilon}{2C_d}\frac{g^2}{\epsilon}\int_p\frac{1}{\Omega^2+p^2}\hat{\gamma}\otimes\hat{\gamma}$$

$$= -\kappa\Omega^\epsilon\frac{\Omega^\epsilon}{2C_d}\frac{g^2}{\epsilon}\Big[\frac{C_{2-\epsilon}}{\epsilon}\Omega^{-\epsilon}+\mathcal{O}(\epsilon)\Big]\hat{\gamma}\otimes\hat{\gamma} = -\frac{\Omega^\epsilon}{2C_d}\frac{g^3}{2\epsilon^2}\hat{\gamma}\otimes\hat{\gamma}+\mathcal{O}(1). \tag{B22}$$

We have calculated all the two-loop vertex diagrams in Figs. 10–14 and shown that the divergent terms take the tensor form of $\hat{\gamma}\otimes\hat{\gamma}$. A sum of all these divergent terms, Eqs. (B5)–(B22), gives the following:

$$[V2] = 2[V2A]+2[V2B]+4[V2C]+4[V2D]+[V2K]+[V2L]+[V2M]+2([V2N]+[V2O])+4[V2a]+2[V2b]+2[V2c]$$

$$= \frac{\Omega^\epsilon}{2C_d}g\Big(\frac{g^2}{8\epsilon}-\frac{g^2}{\epsilon^2}\Big)\hat{\gamma}\otimes\hat{\gamma}+\mathcal{O}(1). \tag{B23}$$

The two-loop vertex counterterm should cancel the divergence in Eq. (B23):

$$\Omega^\epsilon\,\delta^{(2)}\kappa\,\hat{\gamma}\otimes\hat{\gamma}+[V2] = \mathcal{O}(1).$$

From this, we obtain the two-loop vertex counterterm as follows:

$$\Omega^\epsilon\delta^{(2)}\kappa = \frac{\Omega^\epsilon}{2C_d}g\Big(-\frac{g^2}{8\epsilon}+\frac{g^2}{\epsilon^2}\Big). \tag{B24}$$

[1] N. Read and A. W. W. Ludwig, Absence of a metallic phase in random-bond Ising models in two dimensions: Applications to disordered superconductors and paired quantum Hall states, Phys. Rev. B **63**, 024404 (2000).

[2] A. Kitaev, Anyons in an exactly solved model and beyond, Ann. Phys. **321**, 2 (2006).

[3] G. Jackeli and G. Khaliullin, Mott Insulators in the Strong Spin-Orbit Coupling Limit: From Heisenberg to a Quantum Compass and Kitaev Models, Phys. Rev. Lett. **102**, 017205 (2009).

[4] Q. L. He, L. Pan, A. L. Stern, E. C. Burks, X. Che, G. Yin, J. Wang, B. Lian, Q. Zhou, E. S. Choi, K. Murata, X. Kou, Z. Chen, T. Nie, Q. Shao, Y. Fan, S.-C. Zhang, K. Liu, J. Xia, and K. L. Wang, Chiral Majorana fermion modes in a quantum anomalous Hall insulator–superconductor structure, Science **357**, 294 (2017).

[5] M. Kayyalha, D. Xiao, R. Zhang, J. Shin, J. Jiang, F. Wang, Y.-F. Zhao, R. Xiao, L. Zhang, K. M. Fijalkowski, P. Mandal, M. Winnerlein, C. Gould, Q. Li, L. W. Molenkamp, M. H. W. Chan, N. Samarth, and C.-Z. Chang, Absence of evidence for chiral Majorana modes in quantum anomalous Hall-superconductor devices, Science **367**, 64 (2020).

[6] D. Wang, L. Kong, P. Fan, H. Chen, S. Zhu, W. Liu, L. Cao, Y. Sun, S. Du, J. Schneeloch, R. Zhong, G. Gu, L. Fu, H. Ding, and H.-J. Gao, Evidence for Majorana bound states in an iron-based superconductor, Science **362**, 333 (2018).

[7] Y. Huang, F. Setiawan, and J. D. Sau, Disorder-induced half-integer quantized conductance plateau in quantum anomalous Hall insulator-superconductor structures, Phys. Rev. B **97**, 100501(R) (2018).

[8] B. Lian, J. Wang, X.-Q. Sun, A. Vaezi, and S.-C. Zhang, Quantum phase transition of chiral Majorana fermions in the presence of disorder, Phys. Rev. B **97**, 125408 (2018).

[9] M. G. Yamada, Anderson–Kitaev spin liquid, npj Quantum Mater. **5**, 82 (2020).

[10] A. Altland and M. R. Zirnbauer, Nonstandard symmetry classes in mesoscopic normal-superconducting hybrid structures, Phys. Rev. B **55**, 1142 (1997).

[11] S. Cho and M. P. A. Fisher, Criticality in the two-dimensional random-bond Ising model, Phys. Rev. B **55**, 1025 (1997).

[12] T. Senthil and M. P. A. Fisher, Quasiparticle localization in superconductors with spin-orbit scattering, Phys. Rev. B **61**, 9690 (2000).

[13] M. Bocquet, D. Serban, and M. Zirnbauer, Disordered 2D quasiparticles in class D: Dirac fermions with random mass, and dirty superconductors, Nucl. Phys. B **578**, 628 (2000).

[14] J. T. Chalker, N. Read, V. Kagalovsky, B. Horovitz, Y. Avishai, and A. W. W. Ludwig, Thermal metal in network models of a disordered two-dimensional superconductor, Phys. Rev. B **65**, 012506 (2001).

[15] A. Mildenberger, F. Evers, R. Narayanan, A. D. Mirlin, and K. Damle, Griffiths phase in the thermal quantum Hall effect, Phys. Rev. B **73**, 121301(R) (2006).

[16] A. Mildenberger, F. Evers, A. D. Mirlin, and J. T. Chalker, Density of quasiparticle states for a two-dimensional disordered system: Metallic, insulating, and critical behavior in the class-D thermal quantum Hall effect, Phys. Rev. B **75**, 245321 (2007).

[17] F. Evers and A. D. Mirlin, Anderson transitions, Rev. Mod. Phys. **80**, 1355 (2008).

[18] V. Kagalovsky and D. Nemirovsky, Universal Critical Exponent in Class-D Superconductors, Phys. Rev. Lett. **101**, 127001 (2008).

[19] V. Kagalovsky and D. Nemirovsky, Critical fixed points in class-D superconductors, Phys. Rev. B **81**, 033406 (2010).

[20] M. Wimmer, A. R. Akhmerov, M. V. Medvedyeva, J. Tworzydło, and C. W. J. Beenakker, Majorana Bound States Without Vortices in Topological Superconductors with Electrostatic Defects, Phys. Rev. Lett. **105**, 046803 (2010).

[21] M. V. Medvedyeva, J. Tworzydło, and C. W. J. Beenakker, Effective mass and tricritical point for lattice fermions localized by a random mass, Phys. Rev. B **81**, 214203 (2010).

[22] C. R. Laumann, A. W. W. Ludwig, D. A. Huse, and S. Trebst, Disorder-induced Majorana metal in interacting non-Abelian anyon systems, Phys. Rev. B **85**, 161301(R) (2012).

[23] N. Yoshioka, Y. Akagi, and H. Katsura, Learning disordered topological phases by statistical recovery of symmetry, Phys. Rev. B **97**, 205110 (2018).

[24] I. C. Fulga, Y. Oreg, A. D. Mirlin, A. Stern, and D. F. Mross, Temperature Enhancement of Thermal Hall Conductance Quantization, Phys. Rev. Lett. **125**, 236802 (2020).

[25] H. Nishimori, Internal energy, specific heat and correlation function of the bond-random Ising model, Prog. Theor. Phys. **66**, 1169 (1981).

[26] V. S. Dotsenko and V. S. Dotsenko, Critical behaviour of the phase transition in the 2D Ising model with impurities, Adv. Phys. **32**, 129 (1983).

[27] H. Nishimori, Geometry-induced phase transition in the ±J Ising model, J. Phys. Soc. Jpn. **55**, 3305 (1986).

[28] R. Shankar, Exact Critical Behavior of a Random Bond Two-Dimensional Ising Model, Phys. Rev. Lett. **58**, 2466 (1987).

[29] I. A. Gruzberg, N. Read, and A. W. W. Ludwig, Random-bond Ising model in two dimensions: The Nishimori line and supersymmetry, Phys. Rev. B **63**, 104422 (2001).

[30] J. T. Chalker and P. D. Coddington, Percolation, quantum tunnelling and the integer Hall effect, J. Phys. C **21**, 2665 (1988).

[31] V. V. Mkhitaryan and M. E. Raikh, Localization Properties of Random-Mass Dirac Fermions from Real-Space Renormalization Group, Phys. Rev. Lett. **106**, 256803 (2011).

[32] T. Wang, Z. Pan, T. Ohtsuki, I. A. Gruzberg, and R. Shindou, Multicriticality of two-dimensional class-D disordered topological superconductors, Phys. Rev. B **104**, 184201 (2021).

[33] A. W. W. Ludwig, M. P. A. Fisher, R. Shankar, and G. Grinstein, Integer quantum Hall transition: An alternative approach and exact results, Phys. Rev. B **50**, 7526 (1994).

[34] A. Schuessler, P. M. Ostrovsky, I. V. Gornyi, and A. D. Mirlin, Analytic theory of ballistic transport in disordered graphene, Phys. Rev. B **79**, 075405 (2009).

[35] J. Gracey, Computation of the three-loop β-function of the $o(n)$ Gross-Neveu model in minimal subtraction, Nucl. Phys. B **367**, 657 (1991).

[36] J. A. Gracey, T. Luthe, and Y. Schröder, Four loop renormalization of the Gross-Neveu model, Phys. Rev. D **94**, 125028 (2016).

[37] G. Choi, T. A. Ryttov, and R. Shrock, Question of a possible infrared zero in the beta function of the finite-n Gross-Neveu model, Phys. Rev. D **95**, 025012 (2017).

[38] J. H. Pixley, P. Goswami, and S. Das Sarma, Anderson Localization and the Quantum Phase Diagram of Three-Dimensional Disordered Dirac Semimetals, Phys. Rev. Lett. **115**, 076601 (2015).

[39] H. Shapourian and T. L. Hughes, Phase diagrams of disordered Weyl semimetals, Phys. Rev. B **93**, 075108 (2016).

[40] Y.-L. Lee and Y.-W. Lee, Phase diagram of a two-dimensional dirty tilted dirac semimetal, Phys. Rev. B **100**, 075156 (2019).

[41] R. Shindou and S. Murakami, Effects of disorder in three-dimensional Z_2 quantum spin Hall systems, Phys. Rev. B **79**, 045321 (2009).

[42] P. Goswami and S. Chakravarty, Quantum Criticality Between Topological and Band Insulators in $3+1$ Dimensions, Phys. Rev. Lett. **107**, 196803 (2011).

[43] S. Ryu and K. Nomura, Disorder-induced quantum phase transitions in three-dimensional topological insulators and superconductors, Phys. Rev. B **85**, 155138 (2012).

[44] K. Kobayashi, T. Ohtsuki, and K.-I. Imura, Disordered Weak and Strong Topological Insulators, Phys. Rev. Lett. **110**, 236803 (2013).

[45] K. Kobayashi, T. Ohtsuki, K.-I. Imura, and I. F. Herbut, Density of States Scaling at the Semimetal-to-Metal Transition in Three-Dimensional Topological Insulators, Phys. Rev. Lett. **112**, 016402 (2014).

[46] S. Liu, T. Ohtsuki, and R. Shindou, Effect of Disorder in a Three-Dimensional Layered Chern Insulator, Phys. Rev. Lett. **116**, 066401 (2016).

[47] S. Bera, J. D. Sau, and B. Roy, Dirty weyl semimetals: Stability, phase transition, and quantum criticality, Phys. Rev. B **93**, 201302(R) (2016).

[48] X. Luo, B. Xu, T. Ohtsuki, and R. Shindou, Quantum multicriticality in disordered weyl semimetals, Phys. Rev. B **97**, 045129 (2018).

[49] X. Luo, T. Ohtsuki, and R. Shindou, Unconventional scaling theory in disorder-driven quantum phase transition, Phys. Rev. B **98**, 020201(R) (2018).

[50] B. Roy, R.-J. Slager, and V. Juričić, Global Phase Diagram of a Dirty Weyl Liquid and Emergent Superuniversality, Phys. Rev. X **8**, 031076 (2018).

[51] A. C. Potter and P. A. Lee, Multichannel Generalization of Kitaev's Majorana end States and a Practical Route to Realize Them in Thin Films, Phys. Rev. Lett. **105**, 227003 (2010).

[52] B. A. Bernevig, *Topological Insulators and Topological Superconductors* (Princeton University Press, Princeton, NJ, 2013).

[53] A. Altland and B. D. Simons, *Condensed Matter Field Theory* (Cambridge University Press, Cambridge, UK, 2010).

[54] O. Aharony and V. Narovlansky, Renormalization group flow in field theories with quenched disorder, Phys. Rev. D **98**, 045012 (2018).

[55] M. E. Peskin and D. V. Schroeder, *Introduction to Quantum Field Theory* (Westview, Boulder, CO, 1995).

[56] D. J. Amit and V. Martin-Mayor, *Field Theory, Renormalization Group, and Critical Phenomena* (World Scientific, Singapore, 2005).

[57] A. Bondi, G. Curci, G. Paffuti, and P. Rossi, Metric and central charge in the perturbative approach to two-dimensional fermionic models, Ann. Phys. **199**, 268 (1990).

[58] B. Roy and S. Das Sarma, Diffusive quantum criticality in three-dimensional disordered dirac semimetals, Phys. Rev. B **90**, 241112(R) (2014).

[59] S. V. Syzranov, P. M. Ostrovsky, V. Gurarie, and L. Radzihovsky, Critical exponents at the unconventional disorder-

driven transition in a Weyl semimetal, Phys. Rev. B **93**, 155113 (2016).

[60] S. V. Syzranov, V. Gurarie, and L. Radzihovsky, Unconventional localization transition in high dimensions, Phys. Rev. B **91**, 035133 (2015).

[61] M. D. Schwartz, *Quantum Field Theory and the Standard Model* (Cambridge University Press, Cambridge, UK, 2014).

[62] J. T. Chayes, L. Chayes, D. S. Fisher, and T. Spencer, Finite-Size Scaling and Correlation Lengths for Disordered Systems, Phys. Rev. Lett. **57**, 2999 (1986).

[63] M. Dudka, A. A. Fedorenko, V. Blavatska, and Y. Holovatch, Critical behavior of the two-dimensional Ising model with long-range correlated disorder, Phys. Rev. B **93**, 224422 (2016).

[64] B. Roy and S. D. Sarma, Erratum Diffusive quantum criticality in three-dimensional disordered Dirac semimetals [Phys. Rev. B 90, 241112(R) (2014)], Phys. Rev. B **93**, 119911 (2016).

[65] D. J. Gross and A. Neveu, Dynamical symmetry breaking in asymptotically free field theories, Phys. Rev. D **10**, 3235 (1974).

[66] T. Louvet, D. Carpentier, and A. A. Fedorenko, On the disorder-driven quantum transition in three-dimensional relativistic metals, Phys. Rev. B **94**, 220201(R) (2016).